Stable high-voltage operation of oxygen redox in P2-type Na-layered oxide cathode at fast discharging via enhanced kinetics

Bonyoung Ku [a,b,1], Hobin Ahn [a,b,1], Seokjin Lee [a,b], Jinho Ahn [a,b], Myeongeun Choi [a,b], Jungmin Kang [a,b], Hyunyoung Park [a,b], Junseong Kim [a,b], A-Yeon Kim [c], Hun-Gi Jung [c,d], Jung-Keun Yoo [e,*], Jongsoon Kim [a,b,d,*]

[a] Department of Energy Science, Sungkyunkwan University, Suwon 16419, Republic of Korea
[b] SKKU Institute of Energy Science and Technology, Sungkyunkwan University, Suwon 16419, Republic of Korea
[c] Energy Storage Research Center, Korea Institute of Science and Technology, Seoul 02792 Republic of Korea
[d] KIST-SKKU Carbon-Neutral Research Center, Sungkyunkwan University, Suwon 16419, Republic of Korea
[e] Carbon Composites Department, Composites Research Division, Korea Institute of Materials Science (KIMS), 797 Changwondaero, Changwon, Republic of Korea

ARTICLE INFO

ABSTRACT

Sluggish kinetics and structural instability caused by oxygen redox can lead to poor electrochemical performance of cathode materials, resulting in a much lower operating voltage during discharging than charging (especially at high current densities) and poor power-capability. Additionally, undesirable phase transitions during charge/discharge negatively affect the electrochemical performance of oxygen-redox-based P2-type Mn-based layered oxide cathodes. In this study, we demonstrate the successful stabilization of oxygen redox in P2-type Mn-based layered oxide cathodes through the synergy of Cu-Co. Particularly, the discharge operation voltage and energy density during fast charging are significantly enhanced. The average discharge voltage difference of P2-type $Na_{0.67}[Cu_{0.2}Co_{0.2}Mn_{0.6}]O_2$ between 10 and 1000 mA g^{-1} is approximately ~0.18 V, respectively, which is distinctly different from the case of P2-type $Na_{0.67}[Cu_{0.2}Mn_{0.8}]O_2$ showing differences of approximately ~0.36 V under the same conditions. Moreover, after 100 cycles, the discharge capacity of P2-type $Na_{0.67}[Cu_{0.2}Co_{0.2}Mn_{0.6}]O_2$ with oxygen redox is retained to ~93% of the initial capacity, due to both a small volume change during charge/discharge (~0.6%) and successful suppression of undesirable phase transition of P2-OP4. The outcomes of this study underscore the viability of employing oxygen-redox-based P2-type Na-layered oxide as a reasonable method for achieving exceptional high-rate and high-voltage performance.

1. Introduction

Environmental pollution by the indiscriminate use of fossil fuels has been considered as one of the most critical issues in the world.[1,2] Consequently, the importance of eco-friendly energy is emerging, and the development of effective energy storage systems (ESSs) is progressing.[3–7] Li-ion batteries (LIBs) have garnered great attention as one of the most promising EESs owing to their high energy densities. [8–12] Nowadays, demands for LIBs are rapidly growing in large-scale application such as electronic vehicles (EVs) as well as small, portable mobile electronics such as laptops and cellphones. However, the supply of LIB is not keeping up with the explosively growing demands for energy storage systems due to the limited and concentrated Li sources in the earth, which results in large increase of LIB production cost.[13] Thus, the need for new low-cost ESSs is increasing.

Recently, Na-ion batteries (SIBs) have emerged as one of the low-cost alternative to LIBs for large-scale ESSs,[14,15] owing to unlimited Na sources in the sea and the alkali-ion-based reaction mechanism similar to LIBs.[16–18] At present, many researches have focused on development of novel cathode materials for SIBs,[19] such as layered oxides, polyanion compounds, Prussian blue analogue, *etc*. Especially, prismatic-type (P-type) Mn-based layered oxide materials (Na_xMnO_2) have great attention as a promising cathode for SIBs due to their high theoretical capacity.[20] Moreover, it was reported that P2-$Na_x[Mn_{1-y}M_y]O_2$ (M = Mg, Zn, Li, Cu, *etc*.) can exhibit a large available capacity and energy density through not only cationic redox reaction of transition

---

metal (TM) ions but also anionic redox reaction of oxygen anions.[21] However, the oxygen redox reaction (OR) accompanies negative effects on electrochemical properties, such as severely low operation voltage during discharge (especially at high current densities), by sluggish kinetics and structural instability, which should be solved for practical application of OR-based P2-Na$_x$[Mn$_{1-y}$M$_y$]O$_2$ as the cathode for SIBs.[22] Moreover, it was reported that most of OR-based P2-Na$_x$[Mn$_{1-y}$M$_y$]O$_2$ experience the undesirable phase transition from P2-type structure to octahedral-type (O-type) structure on charging, which can be a reason of poor electrochemical performances of OR-based P2-Na$_x$[Mn$_{1-y}$M$_y$]O$_2$.[23] Although it was reported that Cu-based P2-Na$_x$[Mn$_{1-y}$M$_y$]O$_2$ materials can deliver OR during charge/discharge without P2-OP4 phase transition, their OR on discharging occurred at a lower voltage than those on charging, and the voltage gap of OR between the charge and discharge processes became larger at higher current densities.[24] To enhance the OR kinetics during discharging process, we focused on the method to improve the electronic and ionic conductivities on fully Na-deintercalated P2-Na$_x$[Mn$_{1-y}$Cu$_y$]O$_2$. It was reported that the density of states (DOSs) of O $2p$ and Co $3d$ orbitals are overlapped in the layered oxides, which enables outstanding power capability of LiCoO$_2$.[25]

Inspired by these previous researches, we expected Cu-Co cation synergy can successfully enhance the kinetics of high-voltage OR in P2-Na$_x$[Mn$_{1-y}$M$_y$]O$_2$ with no phase transition of P2-OP4 during charge/discharge, and demonstrated it through first-principles calculation and various experiments. At a current density of 10 mA g^{-1} within the voltage range of 2.0–4.6 V (*vs.* Na$^+$/Na), P2-Na$_{0.67}$[Cu$_{0.2}$Co$_{0.2}$Mn$_{0.6}$]O$_2$ exhibited the discharge capacity of ~133 mAh g^{-1}. In particular, its average discharge voltages of ~3.17 V was much higher than P2-Na$_{0.67}$[Cu$_{0.2}$Mn$_{0.8}$]O$_2$ (~2.99 V). Furthermore, at the high current density of 1000 mA g^{-1}, the discharge voltage gap between P2-Na$_{0.67}$[Cu$_{0.2}$Co$_{0.2}$Mn$_{0.6}$]O$_2$ and P2-Na$_{0.67}$[Cu$_{0.2}$Mn$_{0.8}$]O$_2$ was ~0.36 V. P2-Na$_{0.67}$[Cu$_{0.2}$Co$_{0.2}$Mn$_{0.6}$]O$_2$ exhibited ~1.4 times higher energy density at 1000 mA g^{-1} than P2-Na$_{0.67}$[Cu$_{0.2}$Mn$_{0.8}$]O$_2$. These results clearly indicated the enhanced OR kinetics in P2-Na$_{0.67}$[Cu$_{0.2}$Co$_{0.2}$Mn$_{0.6}$]O$_2$, which was also backed up through first-principles calculation to compare the theoretical DOSs and Na$^+$ diffusion barrier energies between the fully Na-deintercalated P2-Na$_0$[Cu$_{0.2}$Co$_{0.2}$Mn$_{0.6}$]O$_2$ and P2-Na$_0$[Cu$_{0.2}$Mn$_{0.8}$]O$_2$. In terms of cycle-performances, P2-Na$_{0.67}$[Cu$_{0.2}$Co$_{0.2}$Mn$_{0.6}$]O$_2$ delivered outstanding capacity retention of above 93% for 100 cycles at 100 mA g^{-1} with high Coulombic efficiency (>99%) despite high-voltage OR during charge/discharge, which is supported by the *operando* XRD results showing well retention of the original structure even after OR reaction without P2-OP4 phase transition. In addition, the OR occurrence in P2-Na$_{0.67}$[Cu$_{0.2}$Co$_{0.2}$Mn$_{0.6}$]O$_2$ was confirmed through first-principles calculation and *ex-situ* soft X-ray absorption spectroscopy (sXAS), *etc*.

2. Material and methods

2.1. Synthesis of P2-Na$_{0.67}$[Cu$_{0.2}$Co$_{0.2}$Mn$_{0.6}$]O$_2$ and P2-Na$_{0.67}$[Cu$_{0.2}$Mn$_{0.8}$]O$_2$

P2-Na$_{0.67}$[Cu$_{0.2}$Co$_{0.2-x}$Mn$_{0.6+x}$]O$_2$ (x = 0, 0.1 and 0.2) compounds and P2-Na$_{0.67}$[Cu$_{0.2-x}$Co$_{0.2}$Mn$_{0.6+x}$]O$_2$ (x= 0.1 and 0.2) were prepared using the solid-state method. Na$_2$CO$_3$ (Sigma Aldrich, 99.5%), CuO (Samchun Chemical, 98%), CoC$_2$O$_4$ (Alfa Aesar, 98%) and Mn$_2$O$_3$ (Alfa Aesar, 99%) were used as precursors. 5 mol% of Na$_2$CO$_3$ was additionally added to compensate the loss of sodium during calcination. P2-Na$_{0.67}$[Ni$_{0.2}$Co$_{0.2}$Mn$_{0.6}$]O$_2$ was also prepared using the solid-state method. Na$_2$CO$_3$ (Sigma Aldrich, 99.5%), Ni(OH)$_2$ (Alfa Aesar, 96.3%), CoC$_2$O$_4$ (Alfa Aesar, 98%) and Mn$_2$O$_3$ (Alfa Aesar, 99%) were used as precursors. 5 mol% of Na$_2$CO$_3$ was additionally added to compensate the loss of sodium during calcination. Stoichiometric amounts of the precursors were mixed by high-energy ball milling machine at 400 rpm for 12 h with silicon-nitride balls. After mixing, the homogenous mixed powder was pelletized using a pressure machine and

calcined under air atmosphere at 850 °C for 12 h (heating rate of 2.5 °C min^{-1}).
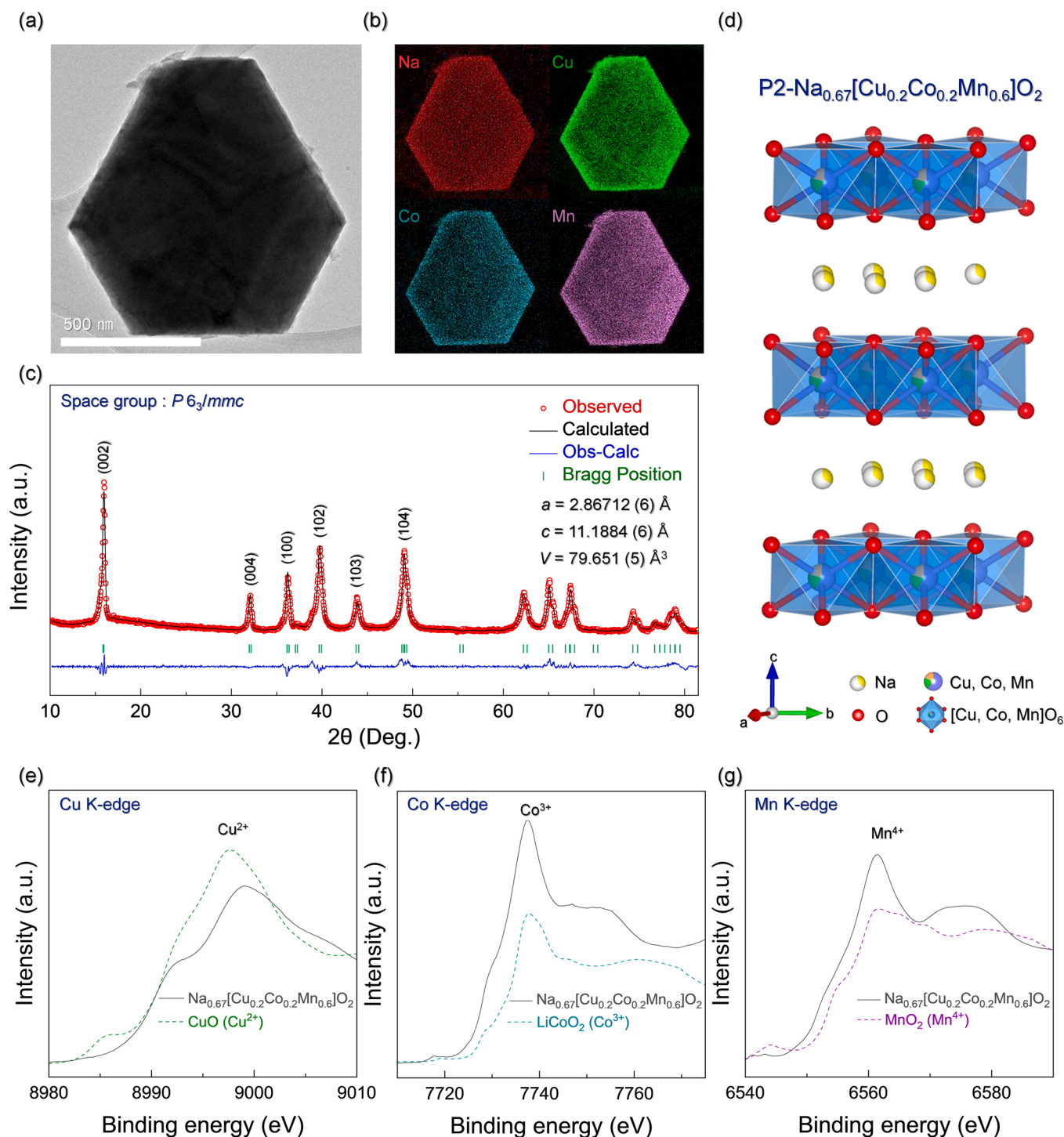
2.2. Materials characterization

The crystal structure of P2-Na$_{0.67}$[Cu$_{0.2}$Co$_{0.2-x}$Mn$_{0.6+x}$]O$_2$ (x = 0 and 0.2) were analyzed using X-ray diffraction (XRD, PANalytical) with Mo Kα radiation (wavelength = 0.70932 Å). The 2θ range was 4.61° to 34.32° with a step size 0.01°. Then, the XRD patterns' angles were transformed using Cu Kα radiation (λ=0.70932 Å) to contrast with previous research. The Fullprof Rietveld program was used to analyze XRD refinement data. The *operando* XRD (o-XRD) patterns were obtained to monitor structural change during charge/discharge at current density of 20 mA g^{-1} within the voltage range 2.0–4.6 V (*vs.* Na$^+$/Na). *Operando* XRD patterns of P2-Na$_{0.67}$[Cu$_{0.2}$Co$_{0.2-x}$Mn$_{0.6+x}$]O$_2$ (x = 0 and 0.2) were measured using an X-ray diffractometer (PANalytical Empyrean) with Cu Kα radiation (wavelength = 1.54178 Å) in the 2θ range of 10° to 82° with a step size 0.013°. The atomic ratio of elements such as Na, Cu, Co and Mn was measured using an inductively coupled plasma emission spectrometer (ICP-AES; OPTIMA 8300, Perkin-Elmer). The FE-SEM (Gemini SEM 560, ZEISS) was utilized at 30 keV to ascertain the morphology of the materials at the National Center for Inter-University Research Facilities (NCIRF) at Seoul National University. TEM images and EDS mappings were measured by FE-TEM; JEM-F200 at the National Center for Inter-University Research Facilities (NCIRF) at Seoul National University. Before conducting the measurements, the samples were dispersed in ethanol using an ultrasonicator. Subsequently, a drop of the suspension was sprayed onto a carbon-coated Cu TEM grid, which was allowed to dry at room temperature overnight for the purpose of ethanol evaporation. Cu K-edge Co K-edge and Mn K-edge were as subjected to *ex-situ* X-ray absorption spectroscopy (XAS) analysis at the 8C Nano XAFS beamline located at the Pohang Accelerator Laboratory (PAL), Cu, Co and Mn metal foil were used as reference spectra. P2-Na$_{0.67}$[Cu$_{0.2}$Mn$_{0.8}$]O$_2$ Cu K-edge and Mn K-edge were as subjected to *ex-situ* X-ray absorption spectroscopy (XAS) analysis at the 10C Wide XAFS beamline located at the Pohang Accelerator Laboratory (PAL), Cu and Mn metal foil were used as reference spectra. The spectra were collected in transmission mode with high electron energy (2.5 GeV) with a 200 mA current condition encompassing the X-ray absorption near edge structure (XANES) and extended X-ray absorption fine structure (EXAFS) regions. Soft X-ray absorption spectroscopy (sXAS) spectra for the O K-edge were measured at the 4D-PES beamline at PAL with a photon energy range of 525-560 eV, utilizing high-energy grating (HEG). The data collected from both XAS and sXAS were subjected to analysis using the Athena software. The samples were prepared in the form of an electrode. X-ray photoelectron spectroscopy (XPS) analysis was measured using an Axis Supra^{TM} (Kratos, UK) at the National Center for Inter-University Research Facilities (NCIRF) at Seoul National University. Continuous-wave electron paramagnetic resonance (CW-EPR) spectra was measured on a EMXplus-9.5/12/P/L system (Bruker) spectrometer with dual mode DM1012 resonator and continuous flow cryostat for EPR (ESR900 OXFORD instruments) in X-band The perpendicular-mode EPR spectra were recorded with a microwave frequency of 9.64 GHz under 50 K using a microwave power of 0.01 mW, modulation amplitude of 10 G, and modulation frequency of 100 kHz. The *ex-situ* CW-EPR spectra observed were normalized based on the mass of cathode materials and measured Q values. EPR measurement samples were sealed in the Ar-filled glove box.

2.3. Electrochemical characterization

P2-Na$_{0.67}$[Cu$_{0.2}$Co$_{0.2-x}$Mn$_{0.6+x}$]O$_2$ (x = 0 and 0.2) electrodes were produced by combining 70 wt% active material, 20 wt% Super P carbon black, and 10 wt% polyvinylidene fluoride (PVDF) using *N*-methyl-2-pyrrolidone (NMP) as the solvent. The mixture was then cast on Al foil and dried overnight under vacuum conditions at 100°C. Once dry, the

electrodes were punched into a disk with a diameter of 10π-mm, and the electrode had a mass loading of approximately 2 mg cm^{-2}. To assemble the half-cells CR2032-type coin cells were used, which included Na metal as the counter electrode, a separator (Whatman GF/F glass fiber), and 1 M NaPF$_6$ in propylene carbonate (PC) and fluoroethylene carbonate (FEC) = 98:2 (v/v) as the electrolyte. The coin cells were assembled in an Ar-filled glove box. Galvanostatic charge/discharge tests were conducted at various current densities (10, 30, 60, 100, 200, 300, 500, 700, and 1000 mA g^{-1} in the voltage range of 2.0–4.6 V (*vs.*

Na$^+$/Na). The charge current density was remained constant at 10.0 mA g^{-1}. The battery cycling tests were performed using an automatic battery charge/discharge test system (WBCS 3000, WonATech). Once the initial charge/discharge process was completed, the cycle-performance was measured at a current density of 100 mA g^{-1}. Differential electron mass spectrometry (Hiden Analytical, UK) was employed to identify the quantities of O$_2$ and CO$_2$ gases produced throughout the electrochemical examination. Coin cells featuring an aperture in the casing were utilized for the DEMS test and placed inside the DEMS cell to

Fig. 1. Material characterization of P2-Na$_{0.67}$[Cu$_{0.2}$Co$_{0.2}$Mn$_{0.6}$]O$_2$: (a) TEM image and (b) TEM-EDS mapping results (atomic ratio of Na: Cu: Co: Mn = 0.335: 1: 1: 3). (c) XRD pattern and Rietveld refinement results of P2-type Na$_{0.67}$[Cu$_{0.2}$Co$_{0.2}$Mn$_{0.6}$]O$_2$ (R$_p$ = 5.30%, R$_{wp}$ = 6.94%, χ^2 = 2.98%). (d) Crystal structure of P2-type Na$_{0.67}$[Cu$_{0.2}$Co$_{0.2}$Mn$_{0.6}$]O$_2$. Pristine K-edge of (e) Cu, (f) Co, (g) Mn.

facilitate the inflow and outflow of gases. Each cell was connected to the DEMS analysis line, which consisted of an argon (Ar) carrier gas, a mass flow controller, an inlet/outlet gas line for cell connection, and a mass spectrometer. Ar gas (99.999% purity) was employed as the carrier gas, and the gas flow rate was adjusted to 2.5 mL min^{-1}. The internal area of the cell was purged with Ar gas to eliminate any residual impurities. Following the purging process, the cell underwent charging/discharging at a current density of 10 mA g^{-1} within the voltage range of 2.0–4.6 V (*vs.* Na$^+$/Na).

2.4. Computational details

All of the density functional theory (DFT) calculations of P2-Na$_{0.67}$[Cu$_{0.2}$Co$_{0.2}$Mn$_{0.6}$]O$_2$ were conducted by the Vienna Ab Initio Simulation Package (VASP) [26]. The projector-augmented wave (PAW) pseudopotentials were adopted through the plane wave basis embedded in the VASP.[27] The exchange–correlation functional was expressed using the generalized gradient approximation (GGA) of the Perdew–Burke–Ernzerhof (PBE) parameterization.[28] A $2 \times 2 \times 1$ supercell structure of P2-Na$_x$[Cu$_{0.25}$Co$_{0.25}$Mn$_{0.5}$]O$_2$ composition was constructed to evaluate the intrinsic features of P2-Na$_{0.67}$[Cu$_{0.2}$Co$_{0.2}$Mn$_{0.6}$]O$_2$. As the main operation mechanism of cathode materials in the battery cell system follows electrochemical reaction pathway, the oxidation states of each transition metals were considered as a main aspect. The constructed structures were calculated using a $6 \times 6 \times 3$ K-point grid. The localization of the d-orbital in Cu, Co, Mn ions were represented by GGA+U method with U$_{eff}$ of 4.0, 3.4, and 3.9, respectively.[29] The Na$^+$/Va configurations at each composition was generated by CASM software, and maximum of 20 configurations at each composition were calculated by the density functional theory (DFT). [30]

3. Result and discussion

3.1. Morphological and structural properties of P2-Na$_{0.67}$[Cu$_{0.2}$Co$_{0.2}$Mn$_{0.6}$]O$_2$

P2-Na$_{0.67}$[Cu$_{0.2}$Co$_{0.2}$Mn$_{0.6}$]O$_2$ was synthesized through a conventional solid-state reaction method. Through transmission electron microscopy (TEM) and scanning electron microscopy (SEM) analyses at low magnification that depict the overall particle size (Fig. 1a and Fig. S1a), it was verified that P2-Na$_{0.67}$[Cu$_{0.2}$Co$_{0.2}$Mn$_{0.6}$]O$_2$ has the average particle size of ~0.9 μm. Additionally, similar to the TEM images, it was observed that plate-like morphology clearly in the SEM images (Fig. S2). TEM-based energy-dispersive X-ray spectroscopy (EDS) elemental mapping analysis indicates Na, Cu, Co, and Mn elements are homogeneously distributed in P2-Na$_{0.67}$[Cu$_{0.2}$Co$_{0.2}$Mn$_{0.6}$]O$_2$ particles and their atomic ratio is Na: Cu: Co: Mn = 0.67: 0.2: 0.2: 0.6 (Fig. 1b). The atomic ratio was also confirmed through inductively coupled plasma (ICP) analysis (Table S1). To investigate the crystal structure of P2-Na$_{0.67}$[Cu$_{0.2}$Co$_{0.2}$Mn$_{0.6}$]O$_2$, we performed the XRD analysis and Rietveld refinement. As shown in Fig. 1c, P2-Na$_{0.67}$[Cu$_{0.2}$Co$_{0.2}$Mn$_{0.6}$]O$_2$ has a well-ordered hexagonal structure and space group P6$_3$/mmc with no impurities or second phases. Its lattice parameters are $a = b =$ 2.86712(6) Å and c = 11.1884(6) Å, and the detailed structural information, such as atomic coordinate, thermal factor (B$_{iso}$), and occupancy, is tabulated in Table S2. The high accuracy of the Rietveld refinement results is demonstrated by the low values of the reliability factors (R$_p$ = 5.30%, R$_{wp}$ = 6.94%, χ^2 = 2.98%). Fig. 1d shows the illustration on the crystal structure of P2-Na$_{0.67}$[Cu$_{0.2}$Co$_{0.2}$Mn$_{0.6}$]O$_2$ based on the structural information, which indicates the typical P2-type layered structure composed of ABBA oxygen stacking sequence. The oxidation states of TMs in P2-Na$_{0.67}$[Cu$_{0.2}$Co$_{0.2}$Mn$_{0.6}$]O$_2$ were analyzed through synchrotron-based X-ray absorption near edge structure (XANES) analyses (Fig. 1e-g). It was identified that Cu and Co ions in P2-Na$_{0.67}$[Cu$_{0.2}$Co$_{0.2}$Mn$_{0.6}$]O$_2$ have the oxidation states of approximately

+2 and +3, respectively. In terms of Mn ions, its oxidation state is close to +4. It implies that the cationic redox (Cu^{2+}/Cu^{3+}, Co^{3+}/Co^{4+} and Mn^{3+}/Mn^{4+}) and anionic redox (O^{2-}/O$^-$) reactions can be occurred in P2-Na$_{0.67}$[Cu$_{0.2}$Co$_{0.2}$Mn$_{0.6}$]O$_2$ during Na$^+$ de/intercalation. In addition, we prepared P2-Na$_{0.67}$[Cu$_{0.2}$Mn$_{0.8}$]O$_2$ as the same synthesis process, to compare the various electrochemical properties with P2-Na$_{0.67}$[Cu$_{0.2}$Co$_{0.2}$Mn$_{0.6}$]O$_2$. Fig. S3-4 show XRD pattern and SEM image of P2-Na$_{0.67}$[Cu$_{0.2}$Mn$_{0.8}$]O$_2$. It was verified the crystal structure of P2-Na$_{0.67}$[Cu$_{0.2}$Mn$_{0.8}$]O$_2$ consists of the hexagonal structure and space group P6$_3$/mmc and its particle size is ~0.95 μm (Fig. S1b), which is highly similar to P2-Na$_{0.67}$[Cu$_{0.2}$Co$_{0.2}$Mn$_{0.6}$]O$_2$.[31] The detailed structural information of P2-Na$_{0.67}$[Cu$_{0.2}$Mn$_{0.8}$]O$_2$ was arranged in Table S3. In addition, we compared the Mn K-edge XANES spectra between P2-Na$_{0.67}$[Cu$_{0.2}$Co$_{0.2}$Mn$_{0.6}$]O$_2$ and P2-Na$_{0.67}$[Cu$_{0.2}$Mn$_{0.8}$]O$_2$ (Fig. S4). It was verified that P2-Na$_{0.67}$[Cu$_{0.2}$Co$_{0.2}$Mn$_{0.6}$]O$_2$ exhibited higher oxidation state of Mn ion than P2-Na$_{0.67}$[Cu$_{0.2}$Mn$_{0.8}$]O$_2$, which indicates that the Co-substitution can result in reducing the amount of Mn^{3+} in P2-type Mn-based layered oxide. It is well matched with the previous researches showing that the Co-substitution can help reducing the fraction of Mn^{3+}.[32]

3.2. Enhanced kinetics of oxygen redox in P2-Na$_{0.2}$Co$_{0.2}$Mn$_{0.6}$]O$_2$

To investigate the synergetic effect of Cu-Co cations for enhanced OR kinetics, we performed the various electrochemical tests of P2-Na$_{0.67}$[Cu$_{0.2}$Co$_{0.2}$Mn$_{0.6}$]O$_2$ and P2-Na$_{0.67}$[Cu$_{0.2}$Mn$_{0.8}$]O$_2$ in the voltage range of 2.0–4.6 V (*vs.* Na$^+$/Na). Fig. S4 shows the initial charge/ discharge curve of P2-Na$_{0.67}$[Cu$_{0.2}$Co$_{0.2}$Mn$_{0.6}$]O$_2$ at the current density of 10 mA g^{-1}, and it was verified the initial charge capacity was ~136 mAh g^{-1} corresponding to 0.53 mol Na$^+$ deintercalation by Cu^{2+}/Cu^{3+}, Co^{3+}/Co^{4+} and O^{2-}/O$^-$ redox reactions. In case of P2-Na$_{0.67}$[Cu$_{0.2}$Mn$_{0.8}$]O$_2$, it delivered the initial charge capacity of ~125 mAh g^{-1} with Cu^{2+}/Cu^{3+} and O^{2-}/O$^-$ redox reactions (Fig. S5) at the same conditions.

Moreover, it was revealed the average discharge voltages of P2-Na$_{0.67}$[Cu$_{0.2}$Co$_{0.2}$Mn$_{0.6}$]O$_2$ and P2-Na$_{0.67}$[Cu$_{0.2}$Mn$_{0.8}$]O$_2$ at 10 mA g^{-1} were ~3.17 V and ~2.99 V, respectively. Interestingly, the difference of the average discharge voltage between them was more remarkable at higher current densities. Fig. 2a-b show the discharge profiles of P2-Na$_{0.67}$[Cu$_{0.2}$Co$_{0.2}$Mn$_{0.6}$]O$_2$ and P2-Na$_{0.67}$[Cu$_{0.2}$Mn$_{0.8}$]O$_2$ at the various current densities after the charging process at 10 mA g^{-1}. The average discharge voltages of P2-Na$_{0.67}$[Cu$_{0.2}$Co$_{0.2}$Mn$_{0.6}$]O$_2$ and P2-Na$_{0.67}$[Cu$_{0.2}$Mn$_{0.8}$]O$_2$ are arranged in Fig. 2c. We confirmed the difference of the average discharge voltages between them gets larger and larger with increase of the discharge current density. Even at 1000 mA g^{-1}, especially, the difference was as much as 0.36 V. Moreover, the discharge capacity of P2-Na$_{0.67}$[Cu$_{0.2}$Co$_{0.2}$Mn$_{0.6}$]O$_2$ was ~102 mAh g^{-1} at 1000 mA g^{-1}, which is larger than that of P2-Na$_{0.67}$[Cu$_{0.2}$Mn$_{0.8}$]O$_2$ (~92 mAh g^{-1}) at the same conditions. Conducting repetitive experiments at different current densities to measure the power-capability also showed similar results. In the case of P2-Na$_{0.67}$[Cu$_{0.2}$Mn$_{0.8}$]O$_2$, the specific discharge capacity was 92.15 mAh g^{-1} at the current density of 1000 mA g^{-1}, which is just 67.75% of the capacity measured at 10 mA g^{-1}. On the other hand, in the case of P2-Na$_{0.67}$[Cu$_{0.2}$Co$_{0.2}$Mn$_{0.6}$]O$_2$, the discharge capacities at 10 and 1000 mA g^{-1} were 133.16 and 102.70 mAh g^{-1}, respectively, which indicates the capacity retention of 77.12% at 1000 mA g^{-1} compared to the capacity at 10 mA g^{-1}. (Fig. S7a-b)

As shown in Fig. 2d, we arranged the power-capability results of P2-Na$_{0.67}$[Cu$_{0.2}$Co$_{0.2}$Mn$_{0.6}$]O$_2$ and P2-Na$_{0.67}$[Cu$_{0.2}$Mn$_{0.8}$]O$_2$ based on the energy density, which shows the outstanding power-capability of P2-Na$_{0.67}$[Cu$_{0.2}$Co$_{0.2}$Mn$_{0.6}$]O$_2$ more clearly. These results imply P2-Na$_{0.67}$[Cu$_{0.2}$Co$_{0.2}$Mn$_{0.6}$]O$_2$ exhibited the enhanced kinetics of OR reaction (O^{2-}/O$^-$) than P2-Na$_{0.67}$[Cu$_{0.2}$Mn$_{0.8}$]O$_2$, which is also demonstrated through the various first-principles calculation results. As presented in Fig. 2e-f, we investigated the theoretical Na$^+$ diffusion motion and the required activation barrier energies of fully Na-
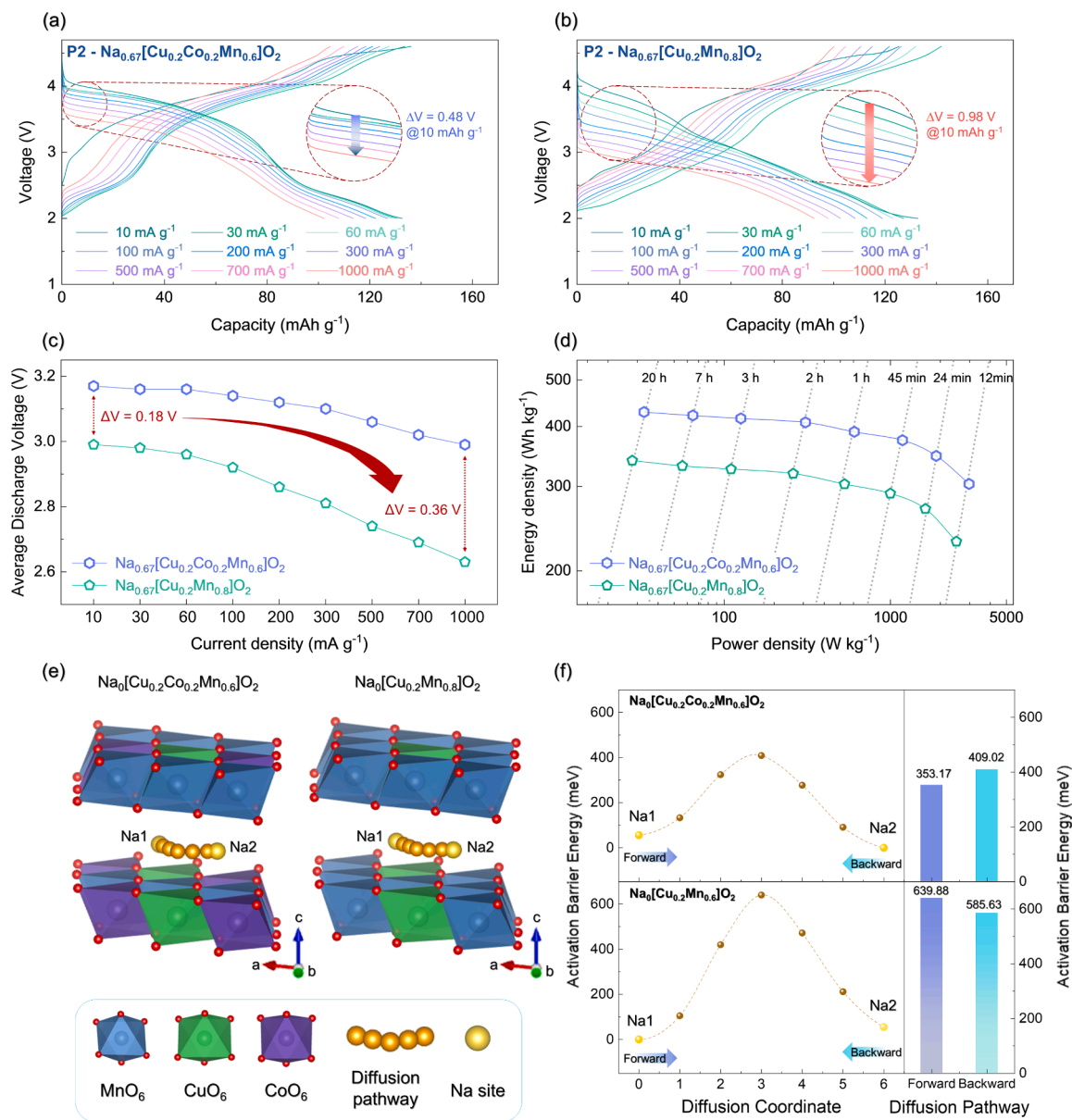
Fig. 2. Electrochemical performance of P2-Na$_{0.67}$[Cu$_{0.2}$Co$_{0.2}$Mn$_{0.6}$]O$_2$ and P2-Na$_{0.67}$[Cu$_{0.2}$Mn$_{0.8}$]O$_2$: Charge/Discharge profiles of (a) P2-Na$_{0.67}$[Cu$_{0.2}$Co$_{0.2}$Mn$_{0.6}$]O$_2$ and (b) P2-Na$_{0.67}$[Cu$_{0.2}$Mn$_{0.8}$]O$_2$ in the voltage range 2.0–4.6 V (*vs.* Na$^+$/Na) at various current densities. (c) Average discharge voltage of P2-Na$_{0.67}$[Cu$_{0.2}$Co$_{0.2}$Mn$_{0.6}$]O$_2$ and P2-Na$_{0.67}$[Cu$_{0.2}$Mn$_{0.8}$]O$_2$ at various current densities. (d) Energy density and power density of P2-Na$_{0.67}$[Cu$_{0.2}$Co$_{0.2}$Mn$_{0.6}$]O$_2$ and P2-Na$_{0.67}$[Cu$_{0.2}$Mn$_{0.8}$]O$_2$ at various current densities. (e) Predicted Na$^+$ diffusion pathway in P2-Na$_{0.67}$[Cu$_{0.2}$Co$_{0.2}$Mn$_{0.6}$]O$_2$ and P2-Na$_{0.67}$[Cu$_{0.2}$Mn$_{0.8}$]O$_2$ and (f) predicted activation barrier energy for Na$^+$ diffusion.

deintercalated P2-Na$_0$[Cu$_{0.2}$Co$_{0.2}$Mn$_{0.6}$]O$_2$ and P2-Na$_0$[Cu$_{0.2}$Mn$_{0.8}$]O$_2$ using nudged elastic band (NEB) method based on first-principles calculation, to compare the Na$^+$ diffusion based on OR during discharge. To investigate the Na$^+$ diffusion kinetics in oxygen redox reaction, the transition metal (TM) ions should be fully oxidized, such as Cu^{3+}, Co^{4+} and Mn^{4+}. Thus, to compare the Na$^+$ diffusion kinetics in oxygen redox reaction between P2-Na$_{0.67}$[Cu$_{0.2}$Co$_{0.2}$Mn$_{0.6}$]O$_2$ and P2-Na$_{0.67}$[Cu$_{0.2}$Mn$_{0.8}$]O$_2$ more clearly, fully Na-deintercalated phases with fully oxidized TM ions were prepared. It was clearly revealed the required Na$^+$ diffusion barrier energy in P2-Na$_0$[Cu$_{0.2}$Co$_{0.2}$Mn$_{0.6}$]O$_2$ (~409.02 meV) is lower than that in P2-Na$_0$[Cu$_{0.2}$Mn$_{0.8}$]O$_2$ (~639.88 meV), which indicates the enhanced OR kinetics in P2-Na$_0$[Cu$_{0.2}$Co$_{0.2}$Mn$_{0.6}$]O$_2$.

The enhanced OR kinetics was also confirmed through additional first-principles calculation on prediction of theoretical DOSs to verify the redox reactions of Cu^{2+}/Cu^{3+}, Co^{3+}/Co^{4+} and O^{2-}/O$^-$ in P2-

Na$_x$[Cu$_{0.2}$Co$_{0.2}$Mn$_{0.6}$]O$_2$. Fig. 3a-b show the changed DOSs and charge densities of P2-Na$_x$[Cu$_{0.2}$Co$_{0.2}$Mn$_{0.6}$]O$_2$ depending on Na contents in the structure. It was verified that Cu^{2+}/Cu^{3+} and Co^{3+}/Co^{4+} redox reactions are occurred during Na$^+$ de/intercalation between P2-Na$_{0.75}$[Cu$_{0.2}$Co$_{0.2}$Mn$_{0.6}$]O$_2$ and P2-Na$_{0.5}$[Cu$_{0.2}$Co$_{0.2}$Mn$_{0.6}$]O$_2$ phases and between P2-Na$_{0.5}$[Cu$_{0.2}$Co$_{0.2}$Mn$_{0.6}$]O$_2$ and P2-Na$_{0.25}$[Cu$_{0.2}$Co$_{0.2}$Mn$_{0.6}$]O$_2$ phases, respectively. The charge densities of O anions neighboring Cu and Co cations were also slightly changed by the effects on Cu^{2+}/Cu^{3+} and Co^{3+}/Co^{4+} redox reactions. And then, OR was occurred during Na$^+$ deintercalation from P2-Na$_{0.25}$[Cu$_{0.2}$Co$_{0.2}$Mn$_{0.6}$]O$_2$, which is confirmed through an unoccupied state of O 2p orbitals in P2-Na$_0$[Cu$_{0.2}$Co$_{0.2}$Mn$_{0.6}$]O$_2$. The various redox reactions occurred in P2-Na$_x$[Cu$_{0.2}$Co$_{0.2}$Mn$_{0.6}$]O$_2$ during Na$^+$ de/intercalation was also demonstrated using the Bader charge calculation (Fig. S6).

Interesting point is the difference of band-gap between fully Na-deintercalated P2-Na$_0$[Cu$_{0.2}$Co$_{0.2}$Mn$_{0.6}$]O$_2$ and P2-Na$_0$[Cu$_{0.2}$Mn$_{0.8}$]O$_2$.
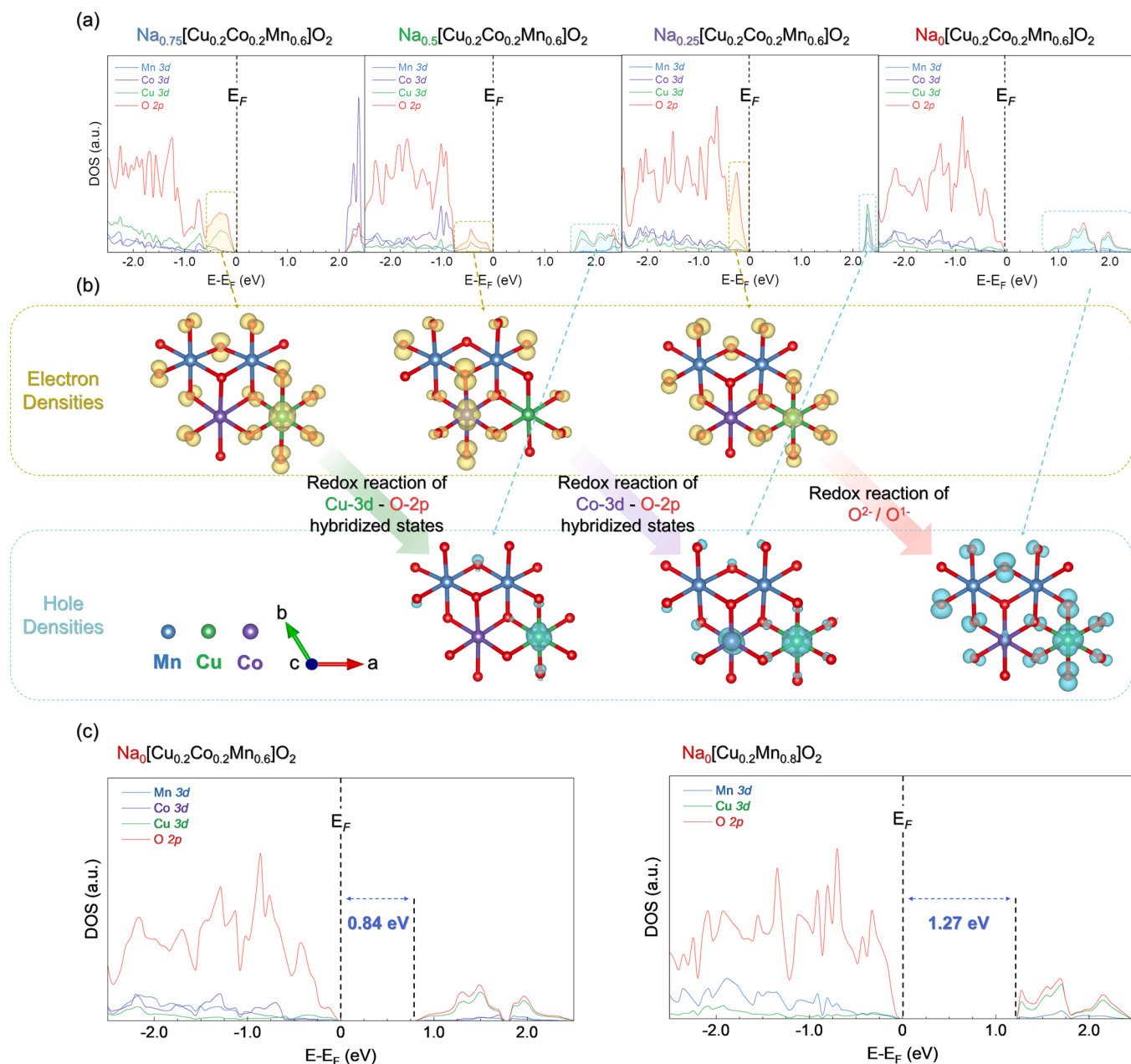
Fig. 3. Calculated density of states and visualized charge density: (a) Projected density of states (pDOS) of Mn-3*d*, Co-3*d*, Cu-3*d* and O-2*p* at P2-Na$_x$[Cu$_{0.2}$Co$_{0.2}$Mn$_{0.6}$]O2 ($0 \leq x \leq 0.75$). (b) The visualized partial charge data of Mn-3*d*, Co-3*d*, Cu-3*d* and O-2*p* collected at P2-Na$_x$[Cu$_{0.2}$Co$_{0.2}$Mn$_{0.6}$]O$_2$ ($0 \leq x \leq 0.75$) (electron densities: yellow dotted box, hole densities: blue botted box). (c) Projected density of states (pDOS) with band-gap of Mn-3*d*, Co-3*d*, Cu-3*d* and O-2*p* of P2-type Na$_0$[Cu$_{0.2}$Co$_{0.2}$Mn$_{0.6}$]O$_2$ and d) Na$_0$[Cu$_{0.2}$Mn$_{0.8}$]O$_2$.

The band-gap allows us to predict the intrinsic electronic conductivities of materials,[33–36] and it was known the lower band-gap indicates the better electronic conductivity.[37,38] Fig. 3c shows the theoretical band-gaps of P2-Na$_0$[Cu$_{0.2}$Co$_{0.2}$Mn$_{0.6}$]O$_2$ and P2-Na$_0$[Cu$_{0.2}$Mn$_{0.8}$]O$_2$ are calculated to be ~0.84 eV and ~1.27 eV, respectively, which indicates the electronic conduction for OR in P2-Na$_0$[Cu$_{0.2}$Co$_{0.2}$Mn$_{0.6}$]O$_2$ during discharge is better than in P2-Na$_0$[Cu$_{0.2}$Mn$_{0.8}$]O$_2$. By these reasons on the enhanced Na$^+$ ionic and electronic conductivities, P2-Na$_{0.67}$[Cu$_{0.2}$Co$_{0.2}$Mn$_{0.6}$]O$_2$ can deliver better OR kinetics than P2-Na$_{0.67}$[Cu$_{0.2}$Mn$_{0.8}$]O$_2$ and the difference of their OR kinetics is more remarkable at high current densities (shown in Fig. 2a-b).

3.3. Outstanding cycle-performance and structural stability of P2-Na$_{0.67}$[Cu$_{0.2}$Co$_{0.2}$Mn$_{0.6}$]O$_2$

In addition, we compared the cycle-performances of P2-Na$_{0.67}$[Cu$_{0.2}$Co$_{0.2}$Mn$_{0.6}$]O$_2$ and P2-Na$_{0.67}$[Cu$_{0.2}$Mn$_{0.8}$]O$_2$. As shown in Fig. 4a, the capacity of P2-Na$_{0.67}$[Cu$_{0.2}$Co$_{0.2}$Mn$_{0.6}$]O$_2$ was retained to ~93% of the initial capacity after 100 cycles at the current density of 100 mA g^{-1}, which is better than the cycle-performance of P2-Na$_{0.67}$[Cu$_{0.2}$Mn$_{0.8}$]O$_2$ showing the capacity retention of ~85% at the same conditions. In particular, their main difference during prolonged cycling is the degree of voltage-decay. It was reported OR can result in the voltage-decay by the structural degradation,[21,39,40] which is considered as an important issue that should be solved for real application of OR-based cathode materials. Fig. 4b shows the average discharge voltages of P2-Na$_{0.67}$[Cu$_{0.2}$Co$_{0.2}$Mn$_{0.6}$]O$_2$ and
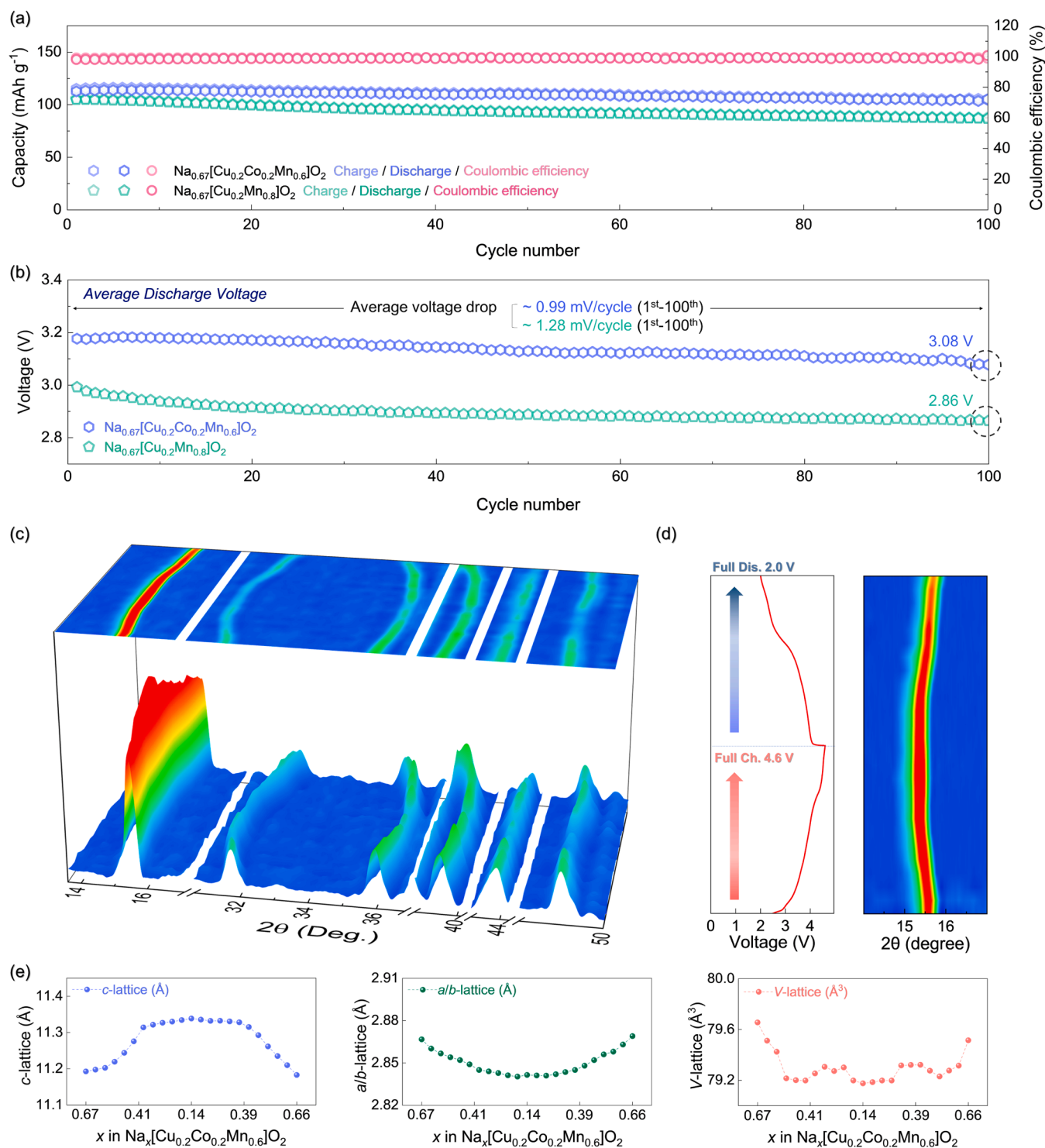
Fig. 4. Structure stability of P2-Na$_{0.67}$[Cu$_{0.2}$Co$_{0.2}$Mn$_{0.6}$]O$_2$: (a) Cycle-performance of P2-Na$_{0.67}$[Cu$_{0.2}$Co$_{0.2}$Mn$_{0.6}$]O$_2$ and P2-Na$_{0.67}$[Cu$_{0.2}$Mn$_{0.8}$]O$_2$ in the voltage range 2.0–4.6 V (*vs.* Na$^+$/Na) during 100 cycles at 100 mA g^{-1} (b) Average discharge voltages for 100 cycles at 100 mA g^{-1} between P2-Na$_{0.67}$[Cu$_{0.2}$Co$_{0.2}$Mn$_{0.6}$]O$_2$ and P2-Na$_{0.67}$[Cu$_{0.2}$Mn$_{0.8}$]O$_2$. (c) *Operando* XRD patterns, (d) voltage profile, magnified views of P2-Na$_{0.67}$[Cu$_{0.2}$Co$_{0.2}$Mn$_{0.6}$]O$_2$ during charge/discharge. (e) Variation of unit cell parameters c (blue points), a/b (green points), and volume (red points).

P2-Na$_{0.67}$[Cu$_{0.2}$Mn$_{0.8}$]O$_2$ for 100 cycles. The voltage decay of P2-Na$_{0.67}$[Cu$_{0.2}$Co$_{0.2}$Mn$_{0.6}$]O$_2$ after 100 cycles was ~99 mV, which is smaller than that of P2-Na$_{0.67}$[Cu$_{0.2}$Mn$_{0.8}$]O$_2$ (~128 mV). Difference of the OR voltage decay between P2-Na$_{0.67}$[Cu$_{0.2}$Co$_{0.2}$Mn$_{0.6}$]O$_2$ and P2-Na$_{0.67}$[Cu$_{0.2}$Mn$_{0.8}$]O$_2$ was more clearly observed in the differential capacity versus voltage (dQ/dV) plots (Fig. S7). These results imply the enhanced structural stability in P2-Na$_{0.67}$[Cu$_{0.2}$Co$_{0.2}$Mn$_{0.6}$]O$_2$ can make

the OR more stably. The difference of cycle-performances between P2-Na$_{0.67}$[Cu$_{0.2}$Co$_{0.2}$Mn$_{0.6}$]O$_2$ and P2-Na$_{0.67}$[Cu$_{0.2}$Mn$_{0.8}$]O$_2$ for 100 cycles at 100 mA g^{-1} was even more evident in comparison of their energy densities (Fig. S8).

To confirm the structural stability of P2-Na$_{0.67}$[Cu$_{0.2}$Co$_{0.2}$Mn$_{0.6}$]O$_2$, we performed the *operando* XRD analysis and investigate the structural changes during Na$^+$ de/intercalation. As shown in Fig. 4c-d, the P2-type

layered structure was well retained without any phase transitions such as P2-OP4 during charge/discharge in the voltage range of 2.0–4.6 V. Through Rietveld refinement, it was also verified the changes in the *c* and *a*(=*b*) lattice parameters of P2-Na$_{0.67}$[Cu$_{0.2}$Co$_{0.2}$Mn$_{0.6}$]O$_2$ during charge/discharge were ~1.2% and ~0.9%, respectively, and the total volume change was just ~0.6% (Fig. 4e). It was reported the strong covalence of Cu-O mitigates the anisotropic changes of other TM-O bonds in the structure,[24,41–43] enabling the maintenance of stable TM-O lattice integrity.[44] Thus, Cu cation can play a crucial role in the suppressing undesired phase transitions within the structure. In case of P2-Na$_{0.67}$[Cu$_{0.2}$Mn$_{0.8}$]O$_2$, it also showed the suppressed phase transition of P2-OP4 during charging to 4.6 V, like P2-Na$_{0.67}$[Cu$_{0.2}$Co$_{0.2}$Mn$_{0.6}$]O$_2$

(Fig. S9). However, the volume change of P2-Na$_{0.67}$[Cu$_{0.2}$Mn$_{0.8}$]O$_2$ during charge/discharge was ~1.8%, which is larger than that of P2-Na$_{0.67}$[Cu$_{0.2}$Co$_{0.2}$Mn$_{0.6}$]O$_2$. Moreover, it was observed that P2-Na$_{0.67}$[Cu$_{0.2}$Co$_{0.2}$Mn$_{0.6}$]O$_2$ showed the slight change in the XRD pattern even after 100 cycles and its morphology was well-preserved, whereas P2-Na$_{0.67}$[Cu$_{0.2}$Mn$_{0.8}$]O$_2$ lost much of its initial XRD pattern after 100 cycles and the intensities of the XRD peaks, especially (002) plane, also highly deteriorated. (Fig. S10-11). These results on the suppression of undesirable phase transitions and the small structural changes indicate the high structural stability of P2-Na$_{0.67}$[Cu$_{0.2}$Co$_{0.2}$Mn$_{0.6}$]O$_2$ by the Cu-Co cation synergy, enabling the stable occurrence of OR .
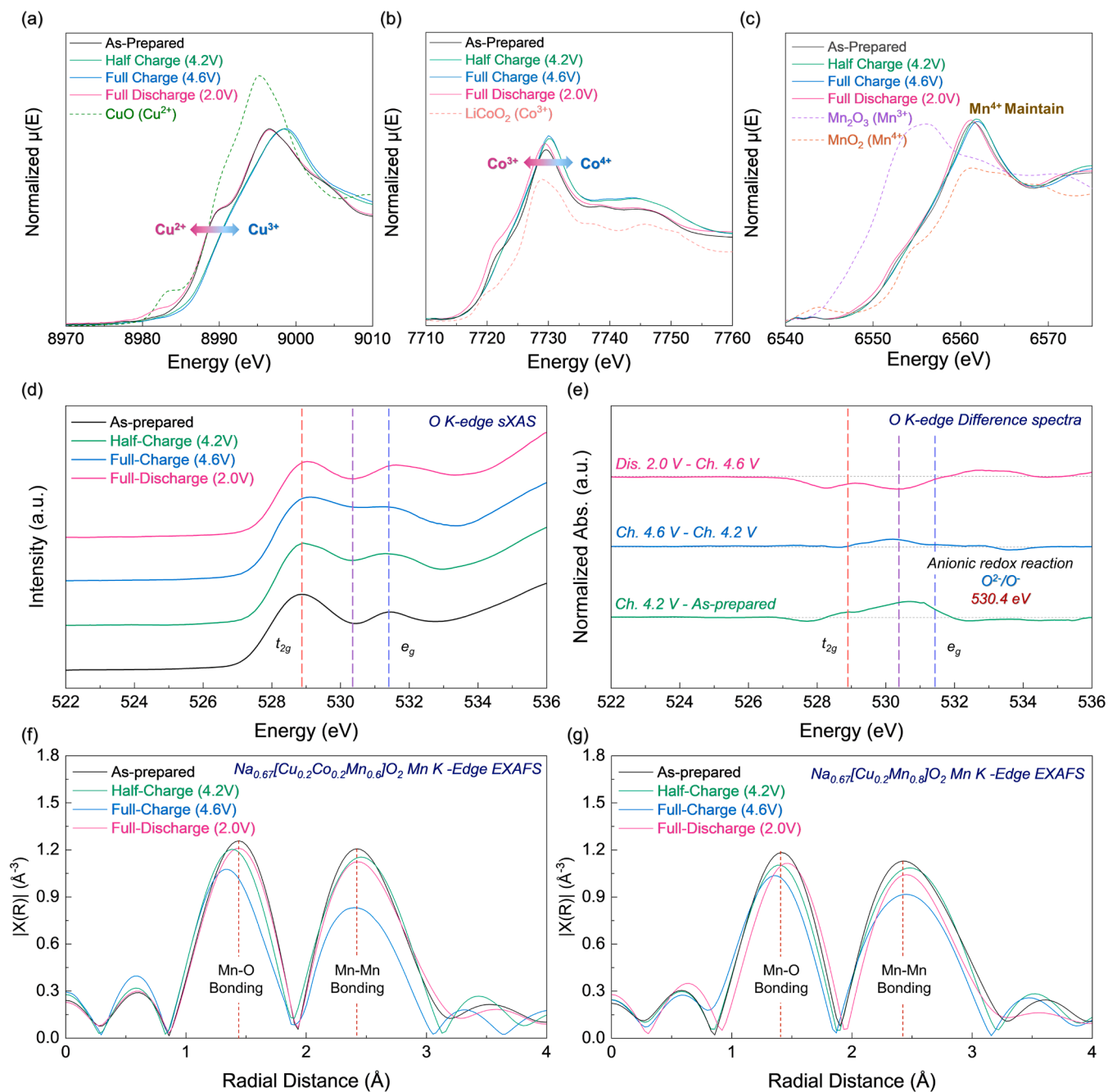
Fig. 5. Redox reaction mechanism of P2-Na$_{0.67}$[Cu$_{0.2}$Co$_{0.2}$Mn$_{0.6}$]O$_2$: *Ex-situ* (a) Cu, (b) Co and (c) Mn K-edge XANES spectra of various state of P2-Na$_{0.67}$[Cu$_{0.2}$Co$_{0.2}$Mn$_{0.6}$]O$_2$. (d) O K-edge sXAS spectra of Na$_{0.67}$[Cu$_{0.2}$Co$_{0.2}$Mn$_{0.6}$]O$_2$ using total fluorescence yield (TFY) mode. (e) O K-edge difference spectra obtained by subtracting *ex-situ* O K-edge spectra. (f) *Ex-situ* Mn K-edge EXAFS analyses of various charge/discharge state of P2-Na$_{0.67}$[Cu$_{0.2}$Co$_{0.2}$Mn$_{0.6}$]O$_2$ and (g) P2-Na$_{0.67}$[Cu$_{0.2}$Mn$_{0.8}$]O$_2$

3.4. Detailed redox reaction mechanism and local structural environment in P2-Na$_{0.67}$[Cu$_{0.2}$Co$_{0.2}$Mn$_{0.6}$]O$_2$

Through *ex-situ* synchrotron-based XANES analyses, we investigated changes of the valence stats on Mn, Cu and Co in P2-Na$_{0.67}$[Cu$_{0.2}$Co$_{0.2}$Mn$_{0.6}$]O$_2$ during charge/discharge. In the Cu K-edge XANES spectra (Fig. 5a), it was observed that the oxidation process of Cu^{2+}/Cu^{3+} was occurred in P2-Na$_{0.67}$[Cu$_{0.2}$Co$_{0.2}$Mn$_{0.6}$]O$_2$ during charge/discharge. Upon charging up to 4.2 V, the oxidation state of Cu cation was changed from +2 to +3, and it was retained without further oxidation during charging from 4.2 V to 4.6 V. Upon discharging back down to 2.0 V, Cu cation was reversibly reduced back to its original +2 oxidation state. In case of the Co K-edge XANES spectra (Fig. 5b), the Co cation was oxidized from +3 to +4 during charging to 4.2 V. And, upon further charging to 4.6 V, the oxidation state of Co^{4+} was retained. During discharge to 2.0 V, the oxidation state of Co was slightly reduced compared to the as-prepared state of +3. As shown in Fig. 5c, it was verified that there is no further oxidation of Mn^{4+} during charging to 4.6 V. Since XANES is known to be greatly influenced by the electronic and structural characteristics of neighboring elements in the local environment,[45,46] the slight change of the Mn K-edge spectrum (especially at the edge-crust) after charge was attributed to the local environmental changes in MnO$_6$ octahedra by OR.[47,48]

Moreover, soft X-ray absorption spectroscopy (sXAS) O K-edge spectra and corresponding difference plots were used to verify the reversible OR in P2-Na$_{0.67}$[Cu$_{0.2}$Co$_{0.2}$Mn$_{0.6}$]O$_2$ (Fig. 5d-e). The unoccupied TM 3d-O 2p t_{2g} hybridized orbitals correspond to the pre-edge peak at approximately 529 eV, while the e_g orbitals are situated near 531.4 eV. During charging to 4.6 V, an increase in absorbance at 530.4 eV was observed in the difference plot, which indicates OR occurrence as originating from the localized feature of the oxidized oxygen state. [49–52] Furthermore, an increase in absorbance at 530.4 eV was observed first in the difference plot during charging from the as-prepared state to 4.2 V. Owing to the strong covalence between Cu and O, hybridization occurs between the Cu 3d and O 2p states, which leads to the onset of OR phenomena from the voltage range of 4.2 V. This is a result of the formation of highly extended TM-O bonds through the strong Cu-O covalence, which in turn strengthens the oxygen lattice and increases the stability of oxidized oxygen intermediates, ultimately enhancing the reversibility of the lattice OR.

Additionally, we have proceeded XPS to further confirm the oxygen redox reaction, and attached O 1s XPS spectra data (Fig. S14). The peaks appeared in the O 1s XPS spectra at 529.5 eV corresponds to O^{2-} anions within the crystalline network, and the signals at 531.7 eV and 533.0 eV are attributed to weakly absorbed species on the surface. These main characteristics of O 1s XPS spectra slightly shifted upon charging to 4.2 V (*vs.* Na$^+$/Na). However, a noticeable change occurs in further charging process to 4.6 V. A series of spectral analysis and fitting procedure of the acquired curves showed the presence of an additional component around 530.5 eV, which is the strong signal of the formal O$_2^{n-}$ species or under-coordinated oxygen atoms, already reported as an evidence of oxygen redox.[53]

Furthermore, we performed the continuous-wave electron paramagnetic resonance (CW-EPR) spectra measurement (based on perpendicular-mode under 50 K) in X-band to further detect the occurrence of oxygen redox reaction during Na+ de/intercalation. It was verified that the EPR signal of as-prepared P2-Na$_{0.67}$[Cu$_{0.2}$Co$_{0.2}$Mn$_{0.6}$]O$_2$ electrode exhibits a single Lorentzian line shape centered at g ≈ 2.000 (Fig. S15), which results from antiferromagnetically coupled Mn^{4+}–O cluster.[54,55] The Mn^{4+} EPR signal was highly broadened during charging to 4.6 V (*vs.* Na$^+$/Na) and its intensity was decreased, which results from the following phenomena: 1) strong electron-electron dipolar interaction between Mn^{4+} and oxidized oxygen (O$_2$)$^{n-}$, 2) Mn^{4+}–O–[TM]$^{4+}$ (such as Co^{4+}) super-exchange couplings. Furthermore, it was verified that the new signal at g ≈ 2.007 gradually appears during charging to 4.6 V, which implies the formation of oxidized (O$_2$)$^{n-}$ by anionic redox reaction of oxygen anion.[56] The EPR signal after discharging to 2.0 V was restored similarly to that of as-prepared P2-Na$_{0.67}$[Cu$_{0.2}$Co$_{0.2}$Mn$_{0.6}$]O$_2$ and the new signal was disappeared, which is related to the reversible reduction of the O anion and the TM cations during the discharging process.[57] Also, it was confirmed that O$_2$ and CO$_2$ gas were released in the high-voltage range by differential electrochemical mass spectrometer (DEMS) (Fig. S16). It is known that the occurrence of oxygen redox reaction in the cathode materials with 3d transition metal (TM) accompanies the structural instability and O$_2$ evolution during charging to the high voltage region, which leads to the poor electrochemical performances of the oxygen-redox-based cathode materials.[8] In the case of P2-Na$_{0.67}$[Cu$_{0.2}$Co$_{0.2}$Mn$_{0.6}$]O$_2$, CO$_2$ gas emission was observed at the high voltage region, which is due to electrolyte decomposition. In particular, it was clearly revealed that O$_2$ gas was negligibly evolved during charging to 4.6 V (*vs.* Na$^+$/Na), which is attributed to the enhanced structural stability of P2-Na$_{0.67}$[Cu$_{0.2}$Co$_{0.2}$Mn$_{0.6}$]O$_2$ by strong covalency of Cu-O bonding. These results can support the reason on superior electrochemical performances of P2-Na$_{0.67}$[Cu$_{0.2}$Co$_{0.2}$Mn$_{0.6}$]O$_2$ with reversible and stable oxygen redox reaction.[58]

In addition, we found the following interesting point from Mn K-edge spectra; the returned Mn K-edge spectra to the as-prepared (OCV) state without further reduction to Mn^{3+} after discharging to 2.0 V, which implies that the negative effect by Jahn-Teller distortion of Mn^{3+} considered as one of the main problems of Mn-based cathode materials is negligible in P2-Na$_{0.67}$[Cu$_{0.2}$Co$_{0.2}$Mn$_{0.6}$]O$_2$.[59,60] On the other hand, P2-Na$_{0.67}$[Cu$_{0.2}$Mn$_{0.8}$]O$_2$ experienced different redox reaction of Mn during charge/discharge from P2-Na$_{0.67}$[Cu$_{0.2}$Co$_{0.2}$Mn$_{0.6}$]O$_2$. As shown in Fig. S17, Mn cation in the 2.0 V-discharged P2-Na$_{0.67}$[Cu$_{0.2}$Mn$_{0.8}$]O$_2$ was more reduced than that in the as-prepared P2-Na$_{0.67}$[Cu$_{0.2}$Mn$_{0.8}$]O$_2$ with Mn^{4+}. Thus, the additional reduction of Mn ions in P2-Na$_{0.67}$[Cu$_{0.2}$Co$_{0.2}$Mn$_{0.6}$]O$_2$ during discharging to 2.0 V (*vs.* Na$^+$/Na) is more difficult than that in P2-Na$_{0.67}$[Cu$_{0.2}$Mn$_{0.8}$]O$_2$. These Mn K-edge XANES results of P2-Na$_{0.67}$[Cu$_{0.2}$Mn$_{0.8}$]O$_2$ and P2-Na$_{0.67}$[Cu$_{0.2}$Co$_{0.2}$Mn$_{0.6}$]O$_2$ can support the difference of their initial Coulombic efficiencies (Fig. 5c and S17). We also performed the extended X-ray absorption fine structure (EXAFS) analyses to investigate the variation of the Mn-O bond length and confirm the preservation of Mn^{4+} in P2-Na$_{0.67}$[Cu$_{0.2}$Co$_{0.2}$Mn$_{0.6}$]O$_2$ (Fig. 5f). As the charging process progressed, the Mn-O bond length in P2-Na$_{0.67}$[Cu$_{0.2}$Co$_{0.2}$Mn$_{0.6}$]O$_2$ slightly decreased and the Mn-O peak intensity changed due to local environmental changes by redox reactions of Cu, Co and O. However, upon discharging to 2.0 V, it was identified that the Mn-O bond mostly returned to its as-prepared state. In case of P2-Na$_{0.67}$[Cu$_{0.2}$Mn$_{0.8}$]O$_2$, however, it was observed that the Mn-O bond length after discharging to 2.0 V was obviously higher than that in the as-prepared state (Fig. 5g), which indicates larger local environmental change of Mn-O in P2-Na$_{0.67}$[Cu$_{0.2}$Mn$_{0.8}$]O$_2$ due to Jahn-Teller distortion of Mn^{3+} than that in P2-Na$_{0.67}$[Cu$_{0.2}$Co$_{0.2}$Mn$_{0.6}$]O$_2$.

3.5. Cu-Co synergy in P2-Na$_{0.67}$[Cu$_{0.2}$Co$_{0.2}$Mn$_{0.6}$]O$_2$

To explore the substitution effects and synergetic effect of Cu and Co in detail, we synthesized additional compounds of P2-Na$_{0.67}$[Cu$_{0.1}$Co$_{0.2}$Mn$_{0.7}$]O$_2$, P2-Na$_{0.67}$[Cu$_{0.2}$Co$_{0.1}$Mn$_{0.7}$]O$_2$, and P2-Na$_{0.67}$[Co$_{0.2}$Mn$_{0.8}$]O$_2$. All three materials were synthesized using the conventional solid-state reaction method, similar to P2-Na$_{0.67}$[Cu$_{0.2}$Co$_{0.2}$Mn$_{0.6}$]O$_2$ and it was confirmed that they possess a perfect P2 phase without any impurities. As shown in Fig. S18-20, P2-Na$_{0.67}$[Cu$_{0.1}$Co$_{0.2}$Mn$_{0.7}$]O$_2$, P2-Na$_{0.67}$[Cu$_{0.2}$Co$_{0.1}$Mn$_{0.7}$]O$_2$, and P2-Na$_{0.67}$[Co$_{0.2}$Mn$_{0.8}$]O$_2$ have a well-ordered hexagonal structure and space group P6$_3$/mmc with no impurities or second phase, and the detailed structural information is tabulated in Table S4-6.

We conducted various electrochemical tests on P2-Na$_{0.67}$[Cu$_{0.1}$Co$_{0.2}$Mn$_{0.7}$]O$_2$, P2-Na$_{0.67}$[Cu$_{0.2}$Co$_{0.1}$Mn$_{0.7}$]O$_2$, and P2-Na$_{0.67}$[Co$_{0.2}$Mn$_{0.8}$]O$_2$ within a voltage range of 2.0–4.6 V (*vs.* Na$^+$/Na).

Fig. S21a illustrates the charge/discharge curves of P2-$Na_{0.67}[Cu_{0.1}Co_{0.2}Mn_{0.7}]O_2$ at various current densities, confirming an initial charge capacity of approximately 112 mAh g^{-1}, corresponding to the deintercalation of 0.44 mol Na$^+$. Similarly, P2-$Na_{0.67}[Cu_{0.2}Co_{0.1}Mn_{0.7}]O_2$ exhibited an initial charge capacity of around 116 mAh g^{-1}, corresponding to 0.45 mol Na$^+$ deintercalation (Fig. S22a). Finally, P2-$Na_{0.67}[Co_{0.2}Mn_{0.8}]O_2$ displayed an initial charge capacity of approximately 120 mAh g^{-1}, corresponding to 0.46 mol Na$^+$ deintercalation (Fig. S23a). Furthermore, Fig. S21b illustrates that P2-$Na_{0.67}[Cu_{0.1}Co_{0.2}Mn_{0.7}]O_2$ retains approximately 90% of its initial capacity after 100 cycles at a current density of 100 mA g^{-1}. P2-$Na_{0.67}[Cu_{0.2}Co_{0.1}Mn_{0.7}]O_2$ showed around 92% of the initial capacity after 100 cycles, while P2-$Na_{0.67}[Co_{0.2}Mn_{0.8}]O_2$ exhibited approximately 83% of the initial capacity after 100 cycles at a current density of 100 mA g^{-1} (Fig. S22b and S23b).

It was reported that a structural transition from P-type to O-type leads to a shorter O-O bond length.[61] Consequently, the energy level of the antibonding orbitals associated with the O-O bond increases, bringing it closer to the Fermi level. This activation stimulates the formation of O-O dimers, thereby further enhancing the activation of the oxygen redox reaction, which enables the large available charge capacity of the oxygen-redox-based cathodes with phase transition of P2-OP4-O2.[53,61,62] However, the phase transition also accompanies large structural change during charge/discharge, which is the reason on the poor electrochemical performances of the oxygen-redox-based cathodes with the phase transition.[63] On the other hand, Cu-substituted P2-type Mn-based layered oxide cathodes don't undergo phase transitions to the O-type, resulting in a relatively small charge capacity compared to the oxygen-redox-based cathodes materials composing of Li and Mg with the phase transition.[64,65] Moreover, the strong Cu-O covalency can enhance structural stability, leading to a stable oxygen redox reaction in Cu-substituted P2-type Mn-based layered oxide cathodes. However, due to high covalency of Cu-O, redox reaction of Cu ions is highly affected by hybridized orbital of Cu 3d and O 2p states,[24] which implies that perfect oxidation from Cu^{2+} ions to Cu^{3+} during charge may be difficult.

For a deeper understanding for the advantages of Cu and Co effect into the crystal structure, we compared the electrochemical performances with the previously mentioned materials. When Co is doped into the structure, it is known that it leads to an increase in electrical conductivity.[66] This offers the advantage of significantly improving both rate performances and structural stability, while simultaneously observing a significant rise in initial discharge voltage. On the other hand, when Cu is doped into the crystal structure, it promotes the covalency of TM-O bonds due to its high electronegativity among 3d transition metals. This suppresses structural distortion and simultaneously activates oxygen redox.[24] Although the initial discharge voltage is slightly decreased due to the Cu substitution, the average discharge voltage is increased according to the maintenance of discharge capacity induced by reduction of oxygen atoms (Fig. S21a and S23a). This is attributed to the enhanced structural stability in the high-voltage region resulting from Cu substitution.[32]

When comparing the average discharge voltage at different current densities to better elucidate the synergistic effect of Cu-Co, it can be observed from Fig. S24 that the average discharge voltage increases with higher current densities as Cu is doped into the structure. Upon comparing P2-$Na_{0.67}[Cu_{0.2}Co_{0.2}Mn_{0.6}]O_2$, P2-$Na_{0.67}[Cu_{0.2}Co_{0.1}Mn_{0.7}]O_2$, and P2-$Na_{0.67}[Cu_{0.2}Mn_{0.8}]O_2$, it can be observed that the initial voltage drop gradually decreases as the amount of doped Co increases (Fig. 2a-b and Fig. S22a). Especially, whereas P2-$Na_{0.67}[Cu_{0.2}Co_{0.2}Mn_{0.6}]O_2$ and P2-$Na_{0.67}[Cu_{0.2}Co_{0.1}Mn_{0.7}]O_2$ initially have similar average discharge voltages, a significant decrease in the average discharge voltage at high current densities can be observed (Fig. S25), which implies Co substitution results in better kinetics for oxygen redox reaction in P2-type Mn-based layered oxide cathode at fast discharging. Among them, P2-$Na_{0.67}[Cu_{0.2}Co_{0.2}Mn_{0.6}]O_2$ exhibits the most

outstanding performance in all aspects, demonstrating excellent synergy effects through the optimal Cu-Co substitution ratio. Moreover, to confirm the particular characteristics of Cu-Co synergy, we synthesized P2-$Na_{0.67}[Ni_{0.2}Co_{0.2}Mn_{0.6}]O_2$ by substituting Cu with Ni and conducted a comparison. P2-$Na_{0.67}[Ni_{0.2}Co_{0.2}Mn_{0.6}]O_2$ exhibits a well-ordered hexagonal structure with the space group P6$_3$/mmc, free from impurities or second phases (Fig. S26), and its detailed structural properties is represented in Table S7. P2-$Na_{0.67}[Ni_{0.2}Co_{0.2}Mn_{0.6}]O_2$ exhibits large charge/discharge capacity due to the Ni$^{2+/4+}$ redox reaction (Fig. S27a). However, the structural instability induced by the phase transition of P2-O2 results in the poor cycle-performance with the capacity retention of ~81% after the initial 20 cycles (Fig. S27b). Moreover, the average discharge voltage was highly decreased when the discharge current density was increased (Fig. S27a). These results highlight that the Cu-Co synergy exhibits distinct characteristics compared to Ni-Co synergy.[65] Furthermore, compared to the energy densities of other P2-type Mn-based layered oxide cathodes,[63,66–71] P2-$Na_{0.67}[Cu_{0.2}Co_{0.2}Mn_{0.6}]O_2$ demonstrates exceptional power capability (as illustrated in Fig. 6 and Table S8). These results indicate that P2-$Na_{0.67}[Cu_{0.2}Co_{0.2}Mn_{0.6}]O_2$ has potential as a promising cathode material for SIBs.

Conclusion

In this study, we demonstrate that P2-$Na_{0.67}[Cu_{0.2}Co_{0.2}Mn_{0.6}]O_2$, based on oxygen redox (OR), can achieve high discharge voltages and energy densities at both low and high current densities due to the enhanced OR kinetics by Cu-Co combination. The average discharge voltages of P2-$Na_{0.67}[Cu_{0.2}Co_{0.2}Mn_{0.6}]O_2$ were ~3.17 V and ~2.99 V at 10 and 1000 mA g^{-1}, respectively, with a gap of just ~0.18 V, which is much smaller than the voltage gap of P2-$Na_{0.67}[Cu_{0.2}Mn_{0.8}]O_2$ under the same conditions (~0.36 V). These results on enhanced OR kinetics were also supported by first-principles calculations, which showed that fully Na-deintercalated P2-$Na_0[Cu_{0.2}Co_{0.2}Mn_{0.6}]O_2$ exhibited both lower activation barrier energy required for Na$^+$ diffusion and lower band gap energy than fully Na-deintercalated P2-$Na_0[Cu_{0.2}Mn_{0.8}]O_2$. Through comparison with other P2-type Mn-based layered oxide cathodes, the excellent power-capability of OR-based P2-$Na_{0.67}[Cu_{0.2}Co_{0.2}Mn_{0.6}]O_2$ was clearly revealed. Moreover, P2-$Na_{0.67}[Cu_{0.2}Co_{0.2}Mn_{0.6}]O_2$ delivered the outstanding cycle-performance, such as the capacity retention of ~93% after 100 cycles with high Coulombic efficiency (>99%), which is attributed not only to small volume change during charge/discharge (~0.6%) but also to suppression of undesirable P2-OP4 phase transition during charge/discharge. We believe that this research represents a meaningful discovery that can contribute to improving OR kinetics for stable high-voltage operation even on fast charging in SIBs.
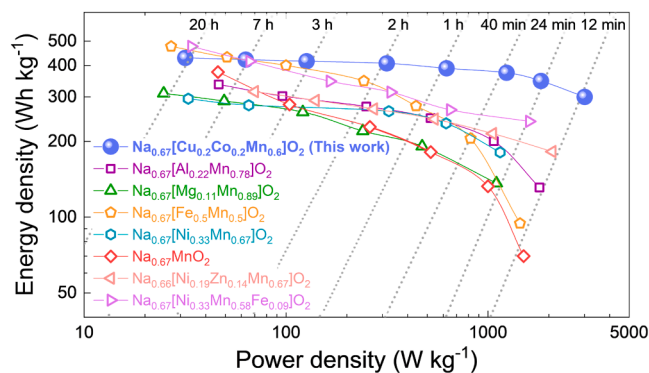

Fig. 6. Comparison of energy and power densities among P2-$Na_{0.67}[Cu_{0.2}Co_{0.2}Mn_{0.6}]O_2$ and other reported Mn-based P2-type layered oxide cathodes for SIBs.

CRediT authorship contribution statement

Bonyoung Ku: Validation, Investigation, Writing – original draft. **Hobin Ahn:** Validation, Formal analysis, Visualization, Writing – original draft. **Seokjin Lee:** Visualization, Investigation. **Jinho Ahn:** Investigation, Methodology. **Myeongeun Choi:** Validation, Methodology. **Jungmin Kang:** Formal analysis, Visualization. **Hyunyoung Park:** Validation, Methodology. **Junseong Kim:** Visualization, Methodology. **A-Yeon Kim:** Investigation, Visualization. **Hun-Gi Jung:** Validation, Visualization. **Jung-Keun Yoo:** Conceptualization, Visualization, Formal analysis, Funding acquisition, Writing – review & editing. **Jongsoon Kim:** Supervision, Project administration, Conceptualization, Funding acquisition, Visualization, Formal analysis, Data curation, Writing – review & editing.

Declaration of Competing Interest

The authors declare the following financial interests/personal relationships which may be considered as potential competing interests:

Jongsoon Kim reports financial support was provided by National Research Foundation of Korea. Jongsoon Kim reports financial support was provided by Korea Institute of Materials Science.

Jongsoon Kim reports financial support was provided by Korea Institute of Science and Technology.

Jongsoon Kim reports financial support was provieded by Korea Institute of Science and Technology Information.

Jung-Keun Yoo reports financial support was provided by National Resesarch Foundation of Korea.

Acknowledgment

Supplementary materials

Supplementary material associated with this article can be found, in the online version, at doi:10.1016/j.ensm.2023.102952.

References

[1] J.P. Holdren, Energy and sustainability, Science (80-.) 315 (2007) 737, https://doi.org/10.1126/SCIENCE.1139792/ASSET/0AA48701-6C62-4B1E-98A7-5C5586A2EE43/ASSETS/GRAPHIC/737-2.GIF.

[2] K. Caldelra, J.F. Kastlng, Insensitivity of global warming potentials to carbon dioxide emission scenarios, Nature (1993) 251–253.

[3] B. Dunn, H. Kamath, J.M. Tarascon, Electrical energy storage for the grid: A battery of choices, Science (80-.) 334 (2011) 928–935, https://doi.org/10.1126/science.1212741.

[4] J.B. Goodenough, How we made the Li-ion rechargeable battery: Progress in portable and ubiquitous electronics would not be possible without rechargeable batteries. John B. Goodenough recounts the history of the lithium-ion rechargeable battery, Nat. Electron. 1 (2018) 204, https://doi.org/10.1038/s41928-018-0048-6.

[5] Y. Lyu, X. Wu, K. Wang, Z. Feng, T. Cheng, Y. Liu, M. Wang, R. Chen, L. Xu, J. Zhou, Y. Lu, B. Guo, An overview on the advances of LiCoO2 cathodes for lithium-ion batteries, Adv. Energy Mater. 11 (2021) 1–29, https://doi.org/10.1002/aenm.202000982.

[6] M. Armand, J.-M. Tarascon, Building better batteries, Nature 451 (2008) 652–657.

[7] T. Kim, W. Choi, H.C. Shin, J.Y. Choi, J.M. Kim, M.S. Park, W.S. Yoon, How to read CV for batteries) Applications of voltammetry in lithium ion battery research, J. Electrochem. Sci. Technol. 11 (2020) 14–25.

[8] Y. Lee, H. Park, M. kyung Cho, J. Ahn, W. Ko, J. Kang, Y.J. Choi, H. Kim, I. Park, W. H. Ryu, J. Hong, J. Kim, Li-Rich Mn–Mg layered oxide as a novel Ni-/Co-free cathode, Adv. Funct. Mater. 32 (2022) 1–13, https://doi.org/10.1002/adfm.202204354.

[9] M. Saubanère, E. McCalla, J.M. Tarascon, M.L. Doublet, The intriguing question of anionic redox in high-energy density cathodes for Li-ion batteries, Energy Environ. Sci. 9 (2016) 984–991, https://doi.org/10.1039/c5ee03048j.

[10] J. Liu, Z. Bao, Y. Cui, E.J. Dufek, J.B. Goodenough, P. Khalifah, Q. Li, B.Y. Liaw, P. Liu, A. Manthiram, Y.S. Meng, V.R. Subramanian, M.F. Toney, V. V. Viswanathan, M.S. Whittingham, J. Xiao, W. Xu, J. Yang, X.Q. Yang, J.G. Zhang, Pathways for practical high-energy long-cycling lithium metal batteries, Nat. Energy. 4 (2019) 180–186, https://doi.org/10.1038/s41560-019-0338-x.

[11] N. Nitta, F. Wu, J.T. Lee, G. Yushin, Li-ion battery materials: present and future, Mater. Today. 18 (2015) 252–264, https://doi.org/10.1016/j.mattod.2014.10.040.

[12] J. Ahn, J. Kang, M. kyung Cho, H. Park, W. Ko, Y. Lee, H.S. Kim, Y.H. Jung, T. Y. Jeon, H. Kim, W.H. Ryu, J. Hong, J. Kim, Selective anionic redox and suppressed structural disordering enabling high-energy and long-life Li-rich layered-oxide cathode, Adv. Energy Mater. 11 (2021), https://doi.org/10.1002/aenm.202102311.

[13] F. Duffner, N. Kronemeyer, J. Tübke, J. Leker, M. Winter, R. Schmuch, Post-lithium-ion battery cell production and its compatibility with lithium-ion cell production infrastructure, Nat. Energy. 6 (2021) 123–134, https://doi.org/10.1038/s41560-020-00748-8.

[14] C. Vaalma, D. Buchholz, M. Weil, S. Passerini, A cost and resource analysis of sodium-ion batteries, Nat. Rev. Mater. 2018 34 (3) (2018) 1–11, https://doi.org/10.1038/natrevmats.2018.13.

[15] Y.S. Hu, Y. Lu, 2019 Nobel Prize for the Li-Ion Batteries and New Opportunities and Challenges in Na-Ion Batteries, ACS Energy Lett 4 (2019) 2689–2690, https://doi.org/10.1021/acsenergylett.9b02190.

[16] J. Kang, J. Ahn, H. Park, W. Ko, Y. Lee, S. Lee, S. Lee, S.K. Jung, J. Kim, Highly stable Fe2+/Ti3+-based fluoride cathode enabling low-cost and high-performance Na-ion batteries, Adv. Funct. Mater. 32 (2022) 1–10, https://doi.org/10.1002/adfm.202201816.

[17] S.W. Kim, D.H. Seo, X. Ma, G. Ceder, K. Kang, Electrode materials for rechargeable sodium-ion batteries: potential alternatives to current lithium-ion batteries, Adv. Energy Mater. 2 (2012) 710–721, https://doi.org/10.1002/aenm.201200026.

[18] N. Yabuuchi, K. Kubota, M. Dahbi, S. Komaba, Research Development on Sodium-Ion Batteries, Chem. Rev. 114 (2014) 11636–11682, https://doi.org/10.1021/cr500192f.

[19] W. Ko, M.-K. Cho, J. Kang, H. Park, J. Ahn, Y. Lee, S. Lee, S. Lee, K. Heo, J. Hong, J.-K. Yoo, J. Kim, Exceptionally increased reversible capacity of O3-type NaCrO2 cathode by preventing irreversible phase transition, Energy Storage Mater. 46 (2022) 289–299, https://doi.org/10.1016/j.ensm.2022.01.023.

[20] R.J. Clément, P.G. Bruce, C.P. Grey, Review—manganese-based P2-type transition metal oxides as sodium-ion battery cathode materials, J. Electrochem. Soc. 162 (2015) A2589–A2604, https://doi.org/10.1149/2.0201514jes.

[21] G. Assat, J.M. Tarascon, Fundamental understanding and practical challenges of anionic redox activity in Li-ion batteries, Nat. Energy. 3 (2018) 373–386, https://doi.org/10.1038/s41560-018-0097-0.

[22] H. Hirsh, Y. Li, J.-H. Cheng, R. Shimizu, M. Zhang, E. Zhao, Y.S. Meng, The negative impact of transition metal migration on oxygen redox activity of layered cathode materials for Na-ion batteries, J. Electrochem. Soc. 168 (2021), 040539, https://doi.org/10.1149/1945-7111/abf96e.

[23] P.F. Wang, Y. You, Y.X. Yin, Y.S. Wang, L.J. Wan, L. Gu, Y.G. Guo, Suppressing the P2–O2 phase transition of Na0.67Mn0.67Ni0.33O2by magnesium substitution for improved sodium-ion batteries, Angew. Chemie - Int. Ed. 55 (2016) 7445–7449, https://doi.org/10.1002/anie.201602202.

[24] C. Cheng, C. Chen, S. Chu, H. Hu, T. Yan, X. Xia, X. Feng, J. Guo, D. Sun, J. Wu, S. Guo, L. Zhang, Enhancing the reversibility of lattice oxygen redox through modulated transition metal–oxygen covalency for layered battery electrodes, Adv. Mater. 34 (2022), 2201152, https://doi.org/10.1002/adma.202201152.

[25] J.B. Goodenough, K.-S. Park, The Li-ion rechargeable battery: a perspective, J. Am. Chem. Soc. 7 (2013) 26, https://doi.org/10.1021/ja3091438.

[26] G. Kresse, J. Furthmüller, Efficiency of ab-initio total energy calculations for metals and semiconductors using a plane-wave basis set, Comput. Mater. Sci. 6 (1996) 15–50, https://doi.org/10.1016/0927-0256(96)00008-0.

[27] P.E. Blöchl, Projector augmented-wave method, Phys. Rev. B. 50 (1994) 17953–17979, https://doi.org/10.1103/PhysRevB.50.17953.

[28] J.P. Perdew, K. Burke, M. Ernzerhof, Generalized gradient approximation made simple, Phys. Rev. Lett. 77 (1996) 3865–3868, https://doi.org/10.1103/PhysRevLett.77.3865.

[29] A. Jain, G. Hautier, S.P. Ong, C.J. Moore, C.C. Fischer, K.A. Persson, G. Ceder, Formation enthalpies by mixing GGA and GGA + U calculations, Phys. Rev. B - Condens. Matter Mater. Phys. 84 (2011) 1–10, https://doi.org/10.1103/PhysRevB.84.045115.

[30] A. Van der Ven, J.C. Thomas, Q. Xu, J. Bhattacharya, Linking the electronic structure of solids to their thermodynamic and kinetic properties, Math. Comput. Simul. 80 (2010) 1393–1410, https://doi.org/10.1016/j.matcom.2009.08.008.

[31] J. Liu, R. Qi, C. Zuo, C. Lin, W. Zhao, N. Yang, J. Li, J. Lu, X. Chen, J. Qiu, M. Chu, M. Zhang, C. Dong, Y. Xiao, H. Chen, F. Pan, Inherent inhibition of oxygen loss by regulating superstructural motifs in anionic redox cathodes, Nano Energy 88 (2021), 106252, https://doi.org/10.1016/j.nanoen.2021.106252.

[32] E.J. Kim, T. Hosaka, K. Kubota, R. Tatara, S. Kumakura, S. Komaba, Effect of Cu substitution in P'2- and P2-type sodium manganese-based oxide, ACS Appl. Energy Mater. 5 (2022) 12999–13010, https://doi.org/10.1021/acsaem.2c02581.

[33] Y. Zhuo, A. Mansouri Tehrani, J. Brgoch, Predicting the band gaps of inorganic solids by machine learning, J. Phys. Chem. Lett. 9 (2018) 1668–1673, https://doi.org/10.1021/acs.jpclett.8b00124.

[34] G. Ceder, Y.M. Chiang, D.R. Sadoway, M.K. Aydinol, Y.I. Jang, B. Huang, Identification of cathode materials for lithium batteries guided by first-principles calculations, Nature 392 (1998) 694–696, https://doi.org/10.1038/33647.

[35] J.P. Perdew, W. Yang, K. Burke, Z. Yang, E.K.U. Gross, M. Scheffler, G.E. Scuseria, T.M. Henderson, I.Y. Zhang, A. Ruzsinszky, H. Peng, J. Sun, E. Trushin, A. Görling, Understanding band gaps of solids in generalized Kohn-Sham theory, Proc. Natl. Acad. Sci. U. S. A. 114 (2017) 2801–2806, https://doi.org/10.1073/pnas.1621352114.

[36] F. Tran, P. Blaha, Accurate band gaps of semiconductors and insulators with a semilocal exchange-correlation potential, Phys. Rev. Lett. 102 (2009) 5–8, https://doi.org/10.1103/PhysRevLett.102.226401.

[37] A.J. Garza, G.E. Scuseria, Predicting band gaps with hybrid density functionals, J. Phys. Chem. Lett. 7 (2016) 4165–4170, https://doi.org/10.1021/acs.jpclett.6b01807.

[38] A. Shaheen, J. Alam, M.S. Anwar, Band structure and electrical conductivity in semiconductors, Mater. Eng. (2010) 1–26.

[39] M. Sathiya, A.M. Abakumov, D. Foix, G. Rousse, K. Ramesha, M. Saubanère, M. L. Doublet, H. Vezin, C.P. Laisa, A.S. Prakash, D. Gonbeau, G. Vantendeloo, J. M. Tarascon, Origin of voltage decay in high-capacity layered oxide electrodes, Nat. Mater. 14 (2015) 230–238, https://doi.org/10.1038/nmat4137.

[40] M.M. Rahman, F. Lin, Oxygen redox chemistry in rechargeable Li-ion and Na-ion batteries, Matter 4 (2021) 490–527, https://doi.org/10.1016/j.matt.2020.12.004.

[41] L. Wang, Y.-G. Sun, L.-L. Hu, J.-Y. Piao, J. Guo, A. Manthiram, J. Ma, A.-M. Cao, Copper-substituted Na 0.67 Ni 0.3Àx Cu x Mn 0.7 O 2 cathode materials for sodium-ion batteries with suppressed P2-O2 phase transition †, (2017). https://doi.org/10.1039/c7ta00880e.

[42] T.R. Chen, T. Sheng, Z.G. Wu, J.T. Li, E.H. Wang, C.J. Wu, H.T. Li, X.D. Guo, B. H. Zhong, L. Huang, S.G. Sun, Cu2+ dual-doped layer-tunnel hybrid Na0.6Mn1-xCuxO2 as a cathode of sodium-ion battery with enhanced structure stability, electrochemical property, and air stability, ACS Appl. Mater. Interfaces 10 (2018) 10147–10156, https://doi.org/10.1021/acsami.8b00614.

[43] Z. Xi, Z. Wang, W. Peng, H. Guo, J. Wang, Effect of copper and iron substitution on the structures and electrochemical properties of LiNi0.8Co0.15Al0.05O2 cathode materials, Energy Sci. Eng. 8 (2020) 1868–1879, https://doi.org/10.1002/ese3.638.

[44] Y. Li, Z. Yang, S. Xu, L. Mu, L. Gu, Y.S. Hu, H. Li, L. Chen, Air-stable copper-based P2-Na7/9Cu2/9Fe1/9Mn2/3O2 as a new positive electrode material for sodium-ion batteries, Adv. Sci. 2 (2015) 1–7, https://doi.org/10.1002/advs.201500031.

[45] J. Yano, V.K. Yachandra, X-ray absorption spectroscopy, Photosynth. Res. 102 (2009) 241–254, https://doi.org/10.1007/s11120-009-9473-8.

[46] S. Lee, W. Ko, H. Park, Y. Lee, J. Kang, J. Ahn, S. Lee, E. Sim, K. Ihm, K.Y. Park, J. Kim, Gradational anionic redox enabling high-energy P2-type Na-layered oxide cathode, Chem. Eng. J. 451 (2023), 138883, https://doi.org/10.1016/j.cej.2022.138883.

[47] H. Lee, S.B. Lim, J.Y. Kim, M. Jeong, Y.J. Park, W.S. Yoon, Characterization and control of irreversible reaction in Li-rich cathode during the initial charge process, ACS Appl. Mater. Interfaces. 10 (2018) 10804–10818, https://doi.org/10.1021/acsami.7b12722.

[48] K. Luo, M.R. Roberts, R. Hao, N. Guerrini, D.M. Pickup, Y.S. Liu, K. Edström, J. Guo, A.V. Chadwick, L.C. Duda, P.G. Bruce, Charge-compensation in 3d-transition-metal-oxide intercalation cathodes through the generation of localized electron holes on oxygen, Nat. Chem. 8 (2016) 684–691, https://doi.org/10.1038/nchem.2471.

[49] M. Amoretti, C. Amsler, G. Bonomi, A. Bouchta, P. Bowe, C. Carraro, C.L. Cesar, M. Chaliton, M.J.T. Collier, M. Doser, V. Filippini, F.S. Fine, A. Fontana, M. C. Fujiwara, R. Funakoshi, P. Genova, J.S. Hangst, R.S. Hayano, M.H. Holzscheiter, L.V. Jørgensen, V. Lagomarsino, R. Landua, D. Lindelöf, E.L. Rizzini, M. Macrì, N. Madsen, G. Manuzio, M. Marchesotti, P. Montagna, H. Pruys, C. Regenfus, P. Riedler, J. Rochet, A. Rotondi, G. Rouleau, G. Testera, A. Variola, T.L. Watson, D.P. Van Der Werf, Production and detection of cold antihydrogen atoms, Nature 419 (2002) 456–459, https://doi.org/10.1038/nature01096.

[50] G. Assat, D. Foix, C. Delacourt, A. Iadecola, R. Dedryvère, J.M. Tarascon, Fundamental interplay between anionic/cationic redox governing the kinetics and thermodynamics of lithium-rich cathodes, Nat. Commun. 8 (2017), https://doi.org/10.1038/s41467-017-02291-9.

[51] E. Zhao, M. Zhang, X. Wang, E. Hu, J. Liu, X. Yu, M. Olguin, T.A. Wynn, Y.S. Meng, K. Page, F. Wang, H. Li, X.Q. Yang, X. Huang, L. Chen, Local structure adaptability through multi cations for oxygen redox accommodation in Li-Rich layered oxides, Energy Storage Mater. 24 (2020) 384–393, https://doi.org/10.1016/j.ensm.2019.07.032.

[52] W.E. Gent, I.I. Abate, W. Yang, L.F. Nazar, W.C. Chueh, Design rules for high-valent redox in intercalation electrodes, Joule 4 (2020) 1369–1397, https://doi.org/10.1016/j.joule.2020.05.004.

[53] X. Rong, J. Liu, E. Hu, Y. Liu, Y. Wang, J. Wu, X. Yu, K. Page, Y.S. Hu, W. Yang, H. Li, X.Q. Yang, L. Chen, X. Huang, Structure-induced reversible anionic redox activity in Na layered oxide cathode, Joule 2 (2018) 125–140, https://doi.org/10.1016/j.joule.2017.10.008.

[54] C. Li, C. Zhao, B. Hu, W. Tong, M. Shen, B. Hu, Unraveling the critical role of Ti substitution in P2-NaxLiyMn1- yO2 cathodes for highly reversible oxygen redox chemistry, Chem. Mater. 32 (2020) 1054–1063, https://doi.org/10.1021/acs.chemmater.9b03765.

[55] X. Sang, X. Xu, Z. Bu, S. Zhai, Y. Sun, M. Ruan, Q. Li, Application of electron paramagnetic resonance in an electrochemical energy storage system, Magnetochemistry 9 (2023), https://doi.org/10.3390/magnetochemistry9030063.

[56] M. Sathiya, J.B. Leriche, E. Salager, D. Gourier, J.M. Tarascon, H. Vezin, Electron paramagnetic resonance imaging for real-time monitoring of Li-ion batteries, Nat. Commun. 6 (2015) 1–7, https://doi.org/10.1038/ncomms7276.

[57] C. Zhao, C. Li, H. Liu, Q. Qiu, F. Geng, M. Shen, W. Tong, J. Li, B. Hu, Coexistence of (O2)n-and trapped molecular O2as the oxidized species in P2-type sodium 3d layered oxide and stable interface enabled by highly fluorinated electrolyte, J. Am. Chem. Soc. 143 (2021) 18652–18664, https://doi.org/10.1021/jacs.1c08614.

[58] H. Ren, Y. Li, Q. Ni, Y. Bai, H. Zhao, C. Wu, Unraveling anionic redox for sodium layered oxide cathodes: breakthroughs and perspectives, Adv. Mater. 34 (2022) 1–34, https://doi.org/10.1002/adma.202106171.

[59] H. Kim, G. Yoon, I. Park, K.Y. Park, B. Lee, J. Kim, Y.U. Park, S.K. Jung, H.D. Lim, D. Ahn, S. Lee, K. Kang, Anomalous Jahn-Teller behavior in a manganese-based mixed-phosphate cathode for sodium ion batteries, Energy Environ. Sci. 8 (2015) 3325–3335, https://doi.org/10.1039/c5ee01876e.

[60] S. Liu, B. Wang, X. Zhang, S. Zhao, Z. Zhang, H. Yu, Reviving the lithium-manganese-based layered oxide cathodes for lithium-ion batteries, Matter 4 (2021) 1511–1527, https://doi.org/10.1016/j.matt.2021.02.023.

[61] W. Zheng, Q. Liu, Z. Wang, Z. Yi, Y. Li, L. Cao, K. Zhang, Z. Lu, Stabilizing the oxygen lattice and reversible oxygen redox in Na-deficient cathode oxides, J. Power Sources. 439 (2019), 227086, https://doi.org/10.1016/j.jpowsour.2019.227086.

[62] J. Hong, W.E. Gent, P. Xiao, K. Lim, D.H. Seo, J. Wu, P.M. Csernica, C.J. Takacs, D. Nordlund, C.J. Sun, K.H. Stone, D. Passarello, W. Yang, D. Prendergast, G. Ceder, M.F. Toney, W.C. Chueh, Metal–oxygen decoordination stabilizes anion redox in Li-rich oxides, Nat. Mater 18 (2019) 256–265, https://doi.org/10.1038/s41563-018-0276-1.

[63] N. Yabuuchi, M. Kajiyama, J. Iwatate, H. Nishikawa, S. Hitomi, R. Okuyama, R. Usui, Y. Yamada, S. Komaba, P2-type Nax [Fe1/2 Mn1/2[O2 made from earth-abundant elements for rechargeable NaÀ batteries, Nat. Mater. 11 (2012) 512–517, https://doi.org/10.1038/nmat3309.

[64] E.J. Kim, T. Hosaka, K. Kubota, R. Tatara, S. Kumakura, S. Komaba, Effect of Cu substitution in P'2-and P2-type sodium manganese-based oxides, Cite This ACS Appl. Energy Mater. (2022) 2022, https://doi.org/10.1021/acsaem.2c02581.

[65] Q. Zhao, F.K. Butt, M. Yang, Z. Guo, X. Yao, M.J.M. Zapata, Y. Zhu, X. Ma, C. Cao, Tuning oxygen redox chemistry of P2-type manganese-based oxide cathode via dual Cu and Co substitution for sodium-ion batteries, Energy Storage Mater. 41 (2021) 581–587, https://doi.org/10.1016/j.ensm.2021.06.029.

[66] C. cheng Fu, J. Wang, Y. Li, G. Liu, T. Deng, Explore the effect of Co doping on P2-Na0.67MnO2 prepared by hydrothermal method as cathode materials for sodium ion batteries, J. Alloys Compd. 918 (2022), 165569, https://doi.org/10.1016/j.jallcom.2022.165569.

[67] W.L. Pang, X.H. Zhang, J.Z. Guo, J.Y. Li, X. Yan, B.H. Hou, H.Y. Guan, X.L. Wu, P2-type Na2/3Mn1-xAlxO2 cathode material for sodium-ion batteries: Al-doped enhanced electrochemical properties and studies on the electrode kinetics, J. Power Sources. 356 (2017) 80–88, https://doi.org/10.1016/j.jpowsour.2017.04.076.

[68] D. Buchholz, C. Vaalma, L.G. Chagas, S. Passerini, Mg-doping for improved long-term cyclability of layered Na-ion cathode materials - The example of P2-type NaxMg0.11Mn0.89O2, J. Power Sources. 282 (2015) 581–585, https://doi.org/10.1016/j.jpowsour.2015.02.069.

[69] S. Kim, K. Min, K. Park, Y-doped P2-type Na0.67Ni0.33Mn0.67O2: A sodium-ion battery cathode with fast charging and enhanced cyclic performance, J. Alloys Compd. 874 (2021) 160027, https://doi.org/10.1016/j.jallcom.2021.160027.

[70] X. Wu, J. Guo, D. Wang, G. Zhong, M.J. McDonald, Y. Yang, P2-type Na0.66Ni0.33-xZnxMn0.67O2 as new high-voltage cathode materials for sodium-ion batteries, J. Power Sources. 281 (2015) 18–26, https://doi.org/10.1016/j.jpowsour.2014.12.083.

[71] Q. Yang, P.F. Wang, J.Z. Guo, Z.M. Chen, W.L. Pang, K.C. Huang, Y.G. Guo, X. L. Wu, J.P. Zhang, Advanced P2-Na2/3Ni1/3Mn7/12Fe1/12O2 cathode material with suppressed P2-O2 phase transition toward high-performance sodium-ion battery, ACS Appl. Mater. Interfaces. 10 (2018) 34272–34282, https://doi.org/10.1021/acsami.8b12204.